Research Article Vol. 32, No. 11 / 20 May 2024 / Optics Express 19854
Optics EXPRESS

Pixelwise immersion factor calibration for underwater hyperspectral imaging instruments

HONGBO LIU,[1,*] NATALIE SUMMERS,[2] YI-CHUN CHEN,[1] HÅVARD SNEFJELLÅ LØVÅS,[3] GEIR JOHNSEN,[2,4] DANIEL KOESTNER,[1] CAMILLA SÆTRE,[1] AND BØRGE HAMRE[1]

[1]*Department of Physics and Technology, University of Bergen, Allégaten 55, Bergen 5007, Norway*
[2]*Centre for Autonomous Marine Operations and Systems (AMOS), Department of Biology, Norwegian University of Science and Technology (NTNU), Trondheim 7018, Norway*
[3]*Centre for Autonomous Marine Operations and Systems (AMOS), Department of Marine Technology, Norwegian University of Science and Technology (NTNU), Trondheim 7491, Norway*
[4]*Department of Arctic Biology, The University Centre in Svalbard (UNIS), Longyearbyen 9171, Norway*
[*]*Hongbo.Liu@uib.no*

Abstract: *In situ* spectral reflectance initially captured at high spatial resolution with underwater hyperspectral imaging (UHI) is effective for classification and quantification in oceanic biogeochemical studies; however, the measured spectral radiance is rarely used as an absolute quantity due to challenges in calibration of UHI instruments. In this paper, a commercial UHI instrument was calibrated for radiometric flat field response and pixelwise immersion effect to support *in situ* measurement of absolute spectral radiance. The radiometric and immersion factor calibrations of the UHI instrument were evaluated quantitatively through comparative experiments with a spectroradiometer and a spectrometer. Results show that the immersion factor of the center pixel of the tested UHI instrument was 1.763 in pure water at 600 nm, and the averaged difference in immersion factor between the center and edge pixel of the UHI instrument in the visible light band was only 1~3% across its half angle field of view of 35° in air. The new calibration coefficients were further used to calculate the spectral radiance of transmitted sunlight through ice algae clusters in sea ice measured by the UHI instrument during an Arctic under-ice bio-optical survey.

1. Introduction

Underwater hyperspectral imaging (UHI) is gaining increasing attention as a promising *in situ* method with high spatial and spectral resolution for oceanic biogeochemical research [1,2]. It has been effectively deployed in seabed mineral classification [3,4], underwater habitat mapping [5–7], and taxonomic studies of benthic organisms [8–11] by leveraging spectral reflectance features of the targets.

In addition to classification and habitat mapping applications, UHI has also been used for the quantification of pigment content in marine biofilms such as the microphytobenthos [12] and ice algae communities. Microalgal communities inhabiting sea ice are an important component of the primary production in Arctic and Antarctic ecosystems [13,14]. However, ice algae are densely distributed at the bottom layer of sea ice, which poses challenges to traditional biomass sampling with ice cores, and constrains the use of airborne or satellite remote sensing techniques [15]. Sunlight penetrating through sea ice containing algae is absorbed by photosynthetic pigments, including chlorophyll *a*, leaving unique signatures in the transmitted light which can be used to approximate ice algae biomass. Underwater towed systems and autonomous underwater vehicles (AUVs) equipped with point-sampling radiance and irradiance sensors have been used

#523641 https://doi.org/10.1364/OE.523641
Journal © 2024 Received 12 Mar 2024; revised 29 Apr 2024; accepted 30 Apr 2024; published 14 May 2024

Optics EXPRESS

for quantitative surveys of algae biomass under sea ice [16,17]. Recently, deployments utilizing UHI technology have shown promise for expanded areal coverage of ice algae biomass mapping [18,19].

In existing UHI applications, the measured reflectance or transmittance spectra are rarely used as absolute quantities, but are often normalized by a reference (e.g., spectrum of a reflectance reference plate or the maximum among the dataset) before classification. However, absolute spectral radiance measured by UHI has the advantage of direct comparison with apparent optical properties and underwater light conditions measured by other radiometric instruments and remote sensing. Particularly for under-ice bio-optical surveys, the transmitted absolute spectral radiance of a transect measured by UHI can be directly related to the downwelling irradiance measured above ice for an accurate estimation of light attenuation and transmission through sea ice across the entire region at high spatial resolution. It provides information of photosynthetically available radiance (PAR) and photosynthetically used radiance (PUR) for a better understanding of the underwater light climate [20–22].

Accurate acquisition of absolute spectral radiance relies on a variety of calibrations, including wavelength, radiometric flat field, smile, and keystone calibration [23]. The hyperspectral sensor of a UHI instrument is conventionally calibrated in air by imaging the aperture of an integrating sphere with uniform light distribution from close distance to fill its entire field of view at a time [24–26]. It is then sealed in a bulky pressure housing with a thick flat optical window for deployment in water, requiring further calibration as a whole, where a larger and more expensive integrating sphere is needed to fit the correspondingly wider front port of the assembled UHI instrument. Furthermore, the calibration coefficients calibrated in air need to be modified to accommodate the changes in solid angle and the interface transmittance when deployed in water, the so-called immersion effect. The immersion effect fundamentally arises from the different refractive index in air and water when light passes through the air-glass and water-glass interfaces, and is usually corrected by an immersion factor for point-sampling radiometers [27,28]. However, unlike point-sampling radiometers which collect incident light from a single viewing angle, pixels of a UHI sensor have different viewing angles. As a result, each pixel of the UHI instrument has a unique immersion factor to be identified experimentally. In addition, angular misalignment between the sensor and housing during assembly introduces geometric errors that need to be considered [29].

In this study, a commercial push-broom UHI instrument with flat glass port was calibrated for radiometric flat field response and pixelwise immersion effect to support *in situ* measurement of absolute spectral radiance. A segmented method for radiometric flat field calibration of the UHI instrument by successively scanning a small-sized integrating sphere was proposed as an inexpensive alternative to the conventional single-shot method. Pixelwise immersion factor of the UHI instrument was first determined theoretically based on calibrated refraction geometry, taking into account sensor tilt due to assembly errors. Meanwhile, an experimental platform was set up for immersion factor calibration reproducing Zibordi's method [27], and the method was extended to calibrate the pixelwise immersion factor of the UHI instrument experimentally in pure water and 35 psu seawater. Then, the performance of the radiometric and immersion factor calibration was evaluated by measurements of an underwater light field whose ground-truth radiance was measured by a calibrated spectroradiometer and a spectrometer. Finally, the verified radiometric calibration coefficient with immersion factor correction was applied to field data from an Arctic under-ice bio-optical survey combining the UHI instrument and other radiometric instruments.

Optics EXPRESS

2. Principles and methods

2.1. Immersion factor of a point-sampling radiance sensor

A typical point-sampling spectroradiometer collects light in a narrow solid angle along its optical axis and analyzes the received radiance at a set of subdivided wavelengths. A simplified model can be used to quantify the received radiant energy, the converted raw digital counts, and the estimated radiance using point-sampling spectroradiometers in air and in water. With the assumption of a small field of view, light passes perpendicularly through all the interfaces along the optical axis. The wavelength dependence is omitted from the following derivation for clarity.

The radiant energy received during exposure time t_a (s) by the spectroradiometer in air is first converted and recorded in proportional raw digital number (DN, in counts) after subtracting the dark signal of the sensor as

$$\mathrm{DN_a} = L_a \cdot \Omega_a \cdot A \cdot T_{ag} \cdot T_{ga} \cdot \rho \cdot t_a, \tag{1}$$

where L_a is the radiance ($\mathrm{mW{\cdot}m^{-2}{\cdot}sr^{-1}}$) of light reaching the optical window of the spectroradiometer in air; Ω_a is the solid angle (sr) of the spectroradiometer in air; A is the light-receiving area ($\mathrm{m^2}$) on the outer surface of the optical window; T_{ag} and T_{ga} are the transmittance at the external and internal air-glass interfaces of the optical window, respectively, and ρ is a composite coefficient that combines the sensor's analog-to-digital conversion coefficient (counts/mJ) and other optical properties of the components.

The raw digital number $\mathrm{DN_a}$ is then used to calculate an estimate of the radiance using a calibration coefficient η_a, which carries both the radiometric and geometric characteristics of the spectroradiometer. By performing a radiometric flat field calibration using a uniform light source and assuming light attenuation in air is negligible, the estimated radiance S_a equals the incident radiance L_a, i.e.,

$$S_a = \frac{\mathrm{DN_a}}{\eta_a \cdot t_a} = L_a, \tag{2}$$

and thus the calibration coefficient is determined as

$$\eta_a = \Omega_a \cdot A \cdot T_{ag} \cdot T_{ga} \cdot \rho. \tag{3}$$

When the spectroradiometer is used in water, the received radiant energy during exposure time t_w (s) is recorded as raw digital number

$$\mathrm{DN_w} = L_w \cdot \Omega_w \cdot A \cdot T_{wg} \cdot T_{ga} \cdot \rho \cdot t_w, \tag{4}$$

where L_w is the radiance ($\mathrm{mW{\cdot}m^{-2}{\cdot}sr^{-1}}$) of light reaching the optical window of the spectroradiometer in water; Ω_w is the solid angle (sr) of the spectroradiometer in water; A is the same light-receiving area ($\mathrm{m^2}$) as in Eq. (1), which depends only on the internal optical design of the spectroradiometer; T_{wg} and T_{ga} are the transmittance at the water-glass and glass-air interfaces of the optical window, respectively; ρ is the same composite coefficient as in Eq. (1).

With the calibration coefficient η_a determined in air, the estimated radiance in water is calculated as

$$S_w = \frac{\mathrm{DN_w}}{\eta_a \cdot t_w} = L_w \cdot \frac{\Omega_w \cdot T_{wg}}{\Omega_a \cdot T_{ag}}, \tag{5}$$

where L_w is not recovered by the estimated radiance S_w, and the latter needs to be modified by an immersion factor, f_{im}, to accommodate the changes in solid angle and transmittance due to

Optics EXPRESS

changes in medium, such that

$$f_{\mathrm{im}} \cdot S_{\mathrm{w}} = f_{\mathrm{im}} \cdot \frac{\mathrm{DN_w}}{\eta_{\mathrm{a}} \cdot t_{\mathrm{w}}} = L_{\mathrm{w}}. \tag{6}$$

And the immersion factor f_{im} can be calculated from Eq. (5) as

$$f_{\mathrm{im}} = \frac{\Omega_{\mathrm{a}} \cdot T_{\mathrm{ag}}}{\Omega_{\mathrm{w}} \cdot T_{\mathrm{wg}}}. \tag{7}$$

The ratio of solid angles and transmittances affecting f_{im} in Eq. (7) can be estimated theoretically by using Snell's law and Fresnel equations [30], respectively. Squaring Snell's law ($n_{\mathrm{a}} \sin\theta_{\mathrm{a}} = n_{\mathrm{w}} \sin\theta_{\mathrm{w}}$) and differentiating it in terms of θ_{a} on both sides gives

$$n_{\mathrm{a}}^2 \, \sin\theta_{\mathrm{a}} \cos\theta_{\mathrm{a}} = n_{\mathrm{w}}^2 \, \sin\theta_{\mathrm{w}} \cos\theta_{\mathrm{w}} \, \frac{d\theta_{\mathrm{w}}}{d\theta_{\mathrm{a}}}. \tag{8}$$

Multiplying each side of this equation by the polar angle $d\theta_{\mathrm{a}}$ and the common azimuth angle $d\phi$, and substituting the differential form of solid angles $d\Omega = \sin\theta \, d\theta \, d\phi$ gives

$$n_{\mathrm{a}}^2 \, \cos\theta_{\mathrm{a}} \, d\Omega_{\mathrm{a}} = n_{\mathrm{w}}^2 \, \cos\theta_{\mathrm{w}} \, d\Omega_{\mathrm{w}}, \tag{9}$$

which is known as Straubel's invariant [31], and the ratio of the solid angles of a general single light beam passing through the air-water interface is thus

$$\frac{\Omega_{\mathrm{a}}}{\Omega_{\mathrm{w}}} = \frac{n_{\mathrm{w}}^2 \, \cos\theta_{\mathrm{w}}}{n_{\mathrm{a}}^2 \, \cos\theta_{\mathrm{a}}}. \tag{10}$$

As to the transmittance at the interface of two media, it is estimated as:

$$T = 1 - \frac{1}{2}(r_{\perp}^2 + r_{\parallel}^2) \tag{11}$$

where $r_{\perp}$ and $r_{\parallel}$ are amplitude reflection coefficients of the components whose electric fields are perpendicular and parallel to the plane-of-incidence, respectively, and can be calculated as

$$r_{\perp} = \frac{n_{\mathrm{I}} \cos\theta_{\mathrm{I}} - n_{\mathrm{T}} \cos\theta_{\mathrm{T}}}{n_{\mathrm{I}} \cos\theta_{\mathrm{I}} + n_{\mathrm{T}} \cos\theta_{\mathrm{T}}} \tag{12}$$

$$r_{\parallel} = \frac{n_{\mathrm{T}} \cos\theta_{\mathrm{I}} - n_{\mathrm{I}} \cos\theta_{\mathrm{T}}}{n_{\mathrm{I}} \cos\theta_{\mathrm{T}} + n_{\mathrm{T}} \cos\theta_{\mathrm{I}}} \tag{13}$$

where the light passes through a planar interface between two media of refractive indices of incident n_{I} and transmitted n_{T} at the incident angle θ_{I} and the transmitted angle θ_{T} depending on the configured air/glass, water/glass, water/air and vice verse.

With the assumption of a small field of view for the point-sampling spectroradiometer, light passes perpendicularly through the interface such that $\theta_{\mathrm{I}} = \theta_{\mathrm{T}} = 0$ in Eq. (12) and Eq. (13); $\theta_{\mathrm{a}} = \theta_{\mathrm{w}} = 0$ in Eq. (10). Along with the assumption that the refractive index of air $n_{\mathrm{a}} = 1$, Eq. (7) becomes

$$f_{\mathrm{im}} = \frac{n_{\mathrm{w}}^2}{n_{\mathrm{a}}^2} \cdot \frac{n_{\mathrm{a}}(n_{\mathrm{w}} + n_{\mathrm{g}})^2}{n_{\mathrm{w}}(n_{\mathrm{a}} + n_{\mathrm{g}})^2} = \frac{n_{\mathrm{w}}(n_{\mathrm{w}} + n_{\mathrm{g}})^2}{(1 + n_{\mathrm{g}})^2}, \tag{14}$$

which is known as Austin's theoretic immersion factor for in-water radiometers [28] and widely used as reference.

Nonetheless, the simplified model presented in Eq. (1) and Eq. (4) only accounts for single reflection at the interface. In practice, light is reflected multiple times between the inner and

Optics EXPRESS

outer boundaries of the optical window, and a much thicker glass window used for deep-water deployments leads to an increased absorption within the glass. Besides, the nominal refractive index of the optical window is a statistical value and does not always represent actual properties of the glass window on a specific instrument with inhomogeneity of the material and manufacturing deviation. Thus, an experimental approach is advantageous for UHI instruments.

Zibordi [27] experimentally determined the immersion factor of a series of RAMSES spectroradiometers, where a stable illuminating surface with radiance L_s at the bottom of a water tank with increasing water depth was measured by the spectroradiometer fixed above. The recorded raw digital number at water depth $r_{w,k}$ below the height of the spectroradiometer in the water tank filled with water of attenuation coefficient α can be denoted as

$$\mathrm{DN}_{wa,k} = L_s \cdot e^{-\alpha \cdot r_{w,k}} \cdot T_{wa} \cdot \frac{\Omega_w}{\Omega_a} \cdot \Omega_a \cdot A \cdot T_{ag} \cdot T_{ga} \cdot \rho \cdot t_{wa} \tag{15}$$

where light with radiance L_s penetrates the water layer of thickness $r_{w,k}$ and successively passes through the water-air interface before reaching the spectroradiometer. By substituting Eq. (3), the estimated radiance becomes

$$S_{wa,k} = \frac{\mathrm{DN}_{wa,k}}{\eta_a \cdot t_{wa}} = L_s \cdot e^{-\alpha \cdot r_{w,k}} \cdot T_{wa} \cdot \frac{\Omega_w}{\Omega_a}. \tag{16}$$

As the water depth keeps increasing until the front window of the spectroradiometer is fully submerged, the recorded raw digital number is represented as

$$\mathrm{DN}_w = L_s \cdot e^{-\alpha \cdot r_w} \cdot \Omega_w \cdot A \cdot T_{wg} \cdot T_{ga} \cdot \rho \cdot t_w, \tag{17}$$

where the light penetrates the water layer of thickness r_w before reaching the spectroradiometer. By substituting Eq. (3), the estimated radiance becomes

$$S_w = \frac{\mathrm{DN}_w}{\eta_a \cdot t_w} = L_s \cdot e^{-\alpha \cdot r_w} \cdot \frac{\Omega_w \cdot T_{wg}}{\Omega_a \cdot T_{ag}}. \tag{18}$$

Combining Eq. (16) and Eq. (18), the ratio of transmittances at the air-glass and water-glass interfaces can be estimated by

$$\frac{T_{ag}}{T_{wg}} = \frac{1}{T_{wa}} \cdot \frac{S_{wa}}{S_w}, \tag{19}$$

where S_{wa} represents the extrapolated $S_{wa,k}$ via linear regression at a critical water depth where the light penetrates the water layer of thickness r_w but still passes through the water-air and air-glass interfaces. Therefore, the immersion factor is experimentally estimated from Eq. (7) and Eq. (19) as

$$f_{im} = \frac{n_w^2}{n_a^2} \cdot \frac{1}{T_{wa}} \cdot \frac{S_{wa}}{S_w}. \tag{20}$$

2.2. Immersion factor of a push-broom hyperspectral imager

Different from a point-sampling spectroradiometer, such as RAMSES ARC-VIS (SAM 810C, TriOS, Germany), which treats the measured light as a perpendicular single beam, the UHI instrument is a push-broom imager where each pixel measures radiance coming from a different direction as shown in Fig. 1(a), so the immersion factor f_{im} needs to be determined pixel by pixel.

A certain pixel P on the UHI sensor is selected as a general example to analyze the pixelwise immersion effect by tracing the received light beams from air and water as shown in Fig. 1(b). The light path from entering the UHI instrument until being received by pixel P is fixed and independent of the external medium, while the incident angle and solid angle at the external

Optics EXPRESS

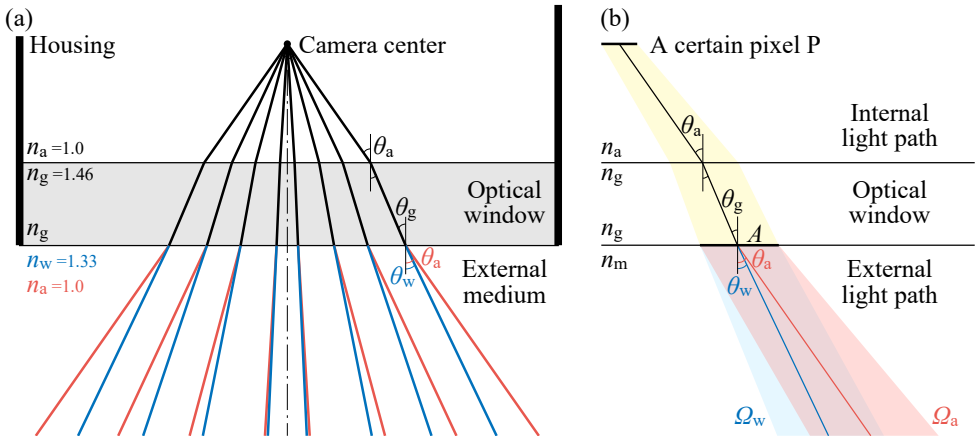

Fig. 1. Optical paths of a UHI instrument measuring radiance in air and water. (a) Different refractions of the measured light in water and air through the air-glass-water interface and the air-glass-air interface forms the immersion effect. Pixels with different viewing angles θ_a have their own immersion factors to be identified. (b) The light path through the light-receiving area A to a certain pixel P on the sensor of the UHI instrument is fixed and independent of the external medium, while the incident angle θ and solid angle Ω at the external interface are determined by the refractive index n_m of the external medium.

interface are determined by the refractive index of the external medium. As a result, the light beams from air and water detected by pixel P share the same light-receiving area A at the outer surface of the optical window, the same transmission angle θ_g through the window glass, and the same angle θ_a (in black) inside the pressure housing in Fig. 1(b). On the other hand, the light beam with radiance L_a from air enters the UHI instrument at the incident angle θ_a (i.e., through the projected area $A \cdot \cos\theta_a$) within the solid angle Ω_a, while the light beam with radiance L_w from water enters the UHI instrument at the incident angle θ_w (i.e., through the projected area $A \cdot \cos\theta_w$) within the solid angle Ω_w due to refraction.

When measuring in air, the radiant energy received by pixel P during exposure time t_a (s) is converted to raw digital number as

$$\mathrm{DN}_a = L_a \cdot \Omega_a \cdot A \cdot \cos\theta_a \cdot T_{ag}(\theta_a) \cdot T_{ga}(\theta_g) \cdot \rho \cdot t_a. \tag{21}$$

The radiometric flat field calibration aims to make the estimated radiance equal to the radiance reaching the UHI instrument in air by

$$S_a = \frac{\mathrm{DN}_a}{\eta_a \cdot t_a} = L_a, \tag{22}$$

which implies a calibration coefficient of

$$\eta_a = \Omega_a \cdot A \cdot \cos\theta_a \cdot T_{ag}(\theta_a) \cdot T_{ga}(\theta_g) \cdot \rho. \tag{23}$$

Similarly, the pixel P receives light reaching the UHI instrument in water and converts it to a raw digital number of

$$\mathrm{DN}_w = L_w \cdot \Omega_w \cdot A \cdot \cos\theta_w \cdot T_{wg}(\theta_w) \cdot T_{ga}(\theta_g) \cdot \rho \cdot t_w. \tag{24}$$

The estimated radiance is then calculated using η_a in Eq. (23) as

$$S_w = \frac{\mathrm{DN}_w}{\eta_a \cdot t_w} = L_w \cdot \frac{\Omega_w \cdot \cos\theta_w \cdot T_{wg}(\theta_w)}{\Omega_a \cdot \cos\theta_a \cdot T_{ag}(\theta_a)}. \tag{25}$$

Optics EXPRESS

By applying Straubel's invariant expressed in Eq. (10) to Eq. (25), the immersion factor of pixel P can be theoretically estimated as

$$f_{\mathrm{im}} = \frac{L_{\mathrm{w}}}{S_{\mathrm{w}}} = \frac{n_{\mathrm{w}}^2}{n_{\mathrm{a}}^2} \cdot \frac{T_{\mathrm{ag}}(\theta_{\mathrm{a}})}{T_{\mathrm{wg}}(\theta_{\mathrm{w}})}, \tag{26}$$

where the angular dependence of solid angles in Eq. (10) is canceled out by the cosine effect of incident light in different media.

The same experimental method is used for the UHI instrument to determine the actual transmittance at the interface for each pixel as for the point-sampling spectroradiometer. It's important to notice that as the water depth in the water tank increases, the field of view of the UHI instrument decreases due to refraction, so the measured area shifts towards the optical axis until the minimum field of view is reached when the UHI instrument is submerged in water.

In Fig. 2, light paths from the water tank bottom to the sensor of the UHI instrument illustrate the misalignment of the pixel P and the measured target points at different water depths $r_{\mathrm{wa},k}$, with the optical window simplified as an interface with zero thickness. When the UHI instrument is submerged in water (i.e., with water depth r_{w}), the pixel P receives light coming from Q on the bottom of the water tank through an optical path length $d_{\mathrm{w}} = r_{\mathrm{w}}/\cos\theta_{\mathrm{w}}$ in water. Assume the target point Q emits light evenly with radiance L_{s} and the attenuation coefficient of the water is α, the estimated radiance is calculated from Eq. (25) as

$$S_{\mathrm{w}} = L_{\mathrm{s}} \cdot e^{-\alpha \cdot d_{\mathrm{w}}} \cdot \frac{\Omega_{\mathrm{w}} \cdot \cos\theta_{\mathrm{w}} \cdot T_{\mathrm{wg}}(\theta_{\mathrm{w}})}{\Omega_{\mathrm{a}} \cdot \cos\theta_{\mathrm{a}} \cdot T_{\mathrm{ag}}(\theta_{\mathrm{a}})}, \tag{27}$$

and by substituting Eq. (10), it becomes

$$S_{\mathrm{w}} = L_{\mathrm{s}} \cdot e^{-\alpha \cdot d_{\mathrm{w}}} \cdot \frac{n_{\mathrm{a}}^2 \cdot T_{\mathrm{wg}}(\theta_{\mathrm{w}})}{n_{\mathrm{w}}^2 \cdot T_{\mathrm{ag}}(\theta_{\mathrm{a}})}. \tag{28}$$

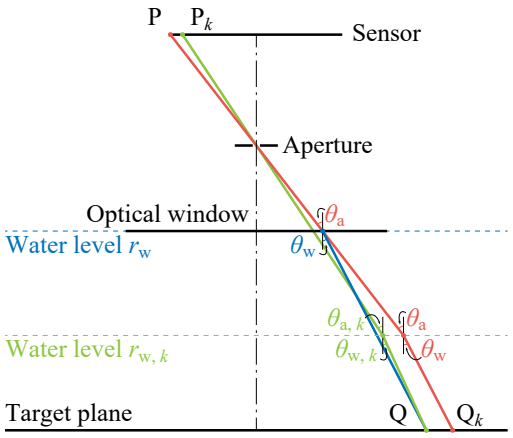

Fig. 2. Misalignment of pixels and target points for the UHI instrument measurements in air and in water due to refraction. When the UHI instrument is submerged in water (i.e., with water depth r_{w}), the pixel P receives light coming from Q, and the transmission angles in water and air are θ_{w} and θ_{a}, respectively. At a certain lower water depth $r_{\mathrm{wa},k}$, pixel P receives light coming from target point Q_k (light path in red), while light comes from target point Q is received by another pixel P_k (light path in green), and the transmission angles in water and air are $\theta_{\mathrm{w},k}$ and $\theta_{\mathrm{a},k}$, respectively.

Optics EXPRESS

At a certain lower water depth $r_{\mathrm{wa},k}$, pixel P receives light coming from target point Q_k (light path in red), while light comes from target point Q is received by another pixel P_k (light path in green). The way to find the corresponding pixel P_k at water depth $r_{\mathrm{wa},k}$ is according to a refraction model presented in detail in Sec. 2.3. As the UHI instrument is in air in this case, rewrite Eq. (21) in terms of the target point Q and pixel P_k as

$$\mathrm{DN}_{\mathrm{wa},k} = L_{\mathrm{wa},k} \cdot \Omega_{\mathrm{a},k} \cdot A_k \cdot \cos\theta_{\mathrm{a},k} \cdot T_{\mathrm{ag}}(\theta_{\mathrm{a},k}) \cdot T_{\mathrm{ga}}(\theta_{\mathrm{g},k}) \cdot \rho_k \cdot t_{\mathrm{wa}}, \tag{29}$$

which implies that the radiometric flat field calibration in air will yield a calibration coefficient of the pixel P_k as

$$\eta_{\mathrm{wa},k} = \Omega_{\mathrm{a},k} \cdot A_k \cdot \cos\theta_{\mathrm{a},k} \cdot T_{\mathrm{ag}}(\theta_{\mathrm{a},k}) \cdot T_{\mathrm{ga}}(\theta_{\mathrm{g},k}) \cdot \rho_k. \tag{30}$$

The estimated radiance is then calculated as

$$S_{\mathrm{wa},k} = \frac{\mathrm{DN}_{\mathrm{wa},k}}{\eta_{\mathrm{wa},k} \cdot t_{\mathrm{wa}}} = L_{\mathrm{wa},k}, \tag{31}$$

where $L_{\mathrm{wa},k}$ is the radiance of light reaching the UHI instrument after passing through an optical path length $d_{\mathrm{w},k} = r_{\mathrm{w},k}/\cos\theta_{\mathrm{w},k}$ in water and crossing the water-air interface at an angle of $\theta_{\mathrm{w},k}$. The transmittance at the water-air interface is defined by the incident and transmitted radiant flux as

$$T_{\mathrm{wa}}(\theta_{\mathrm{w}}) = \frac{\Phi_{\mathrm{a}}}{\Phi_{\mathrm{w}}} = \frac{L_{\mathrm{wa},k}}{L_{\mathrm{s}} \cdot e^{-\alpha \cdot r_{\mathrm{w},k}}} \cdot \frac{\Omega_{\mathrm{a}} \cdot \cos\theta_{\mathrm{a}}}{\Omega_{\mathrm{w}} \cdot \cos\theta_{\mathrm{w}}}. \tag{32}$$

By substituting Eq. (32) and Eq. (10), Eq. (31) becomes

$$S_{\mathrm{wa},k} = L_{\mathrm{s}} \cdot e^{-\alpha \cdot d_{\mathrm{w},k}} \cdot \frac{n_{\mathrm{a}}^2}{n_{\mathrm{w}}^2} \cdot T_{\mathrm{wa}}(\theta_{\mathrm{w},k}). \tag{33}$$

The estimated radiances $S_{\mathrm{wa},k}$ by pixel P_k at different water depths $r_{\mathrm{wa},k}$ are then extrapolated to water depth r_{w} via linear regression as

$$S_{\mathrm{wa}} = L_{\mathrm{s}} \cdot e^{-\alpha \cdot d_{\mathrm{w}}} \cdot \frac{n_{\mathrm{a}}^2}{n_{\mathrm{w}}^2} \cdot T_{\mathrm{wa}}(\theta_{\mathrm{w}}). \tag{34}$$

The ratio of transmittances in Eq. (26) is calculated by dividing Eq. (28) from Eq. (34) as

$$\frac{T_{\mathrm{ag}}(\theta_{\mathrm{a}})}{T_{\mathrm{wg}}(\theta_{\mathrm{w}})} = \frac{1}{T_{\mathrm{wa}}(\theta_{\mathrm{w}})} \cdot \frac{S_{\mathrm{wa}}}{S_{\mathrm{w}}}, \tag{35}$$

and the immersion factor of the pixel P is estimated from Eq. (26) and Eq. (35) as

$$f_{\mathrm{im}} = \frac{n_{\mathrm{w}}^2}{n_{\mathrm{a}}^2} \cdot \frac{1}{T_{\mathrm{wa}}(\theta_{\mathrm{w}})} \cdot \frac{S_{\mathrm{wa}}}{S_{\mathrm{w}}}. \tag{36}$$

2.3. Refraction model and tilt angle correction

The field of view of pixels of the UHI instrument are significantly affected by the refraction of light in different media. In addition, the camera fixed in the housing is usually tilted due to assembly errors, which also has an impact on the imaging geometry of the pixels. A refraction model is established to simulate the spatial coverage of each pixel of the UHI instrument. The UHI instrument is modeled as a pinhole camera, with the camera center located r_{a} away from the inner side of the optical window as shown in Fig. 3(a).

The thickness of the optical window is r_{g} and the target is located r_{m} away from the outer side of the optical window. The tilt angles of the camera and the housing along the line scan slit of

Optics EXPRESS

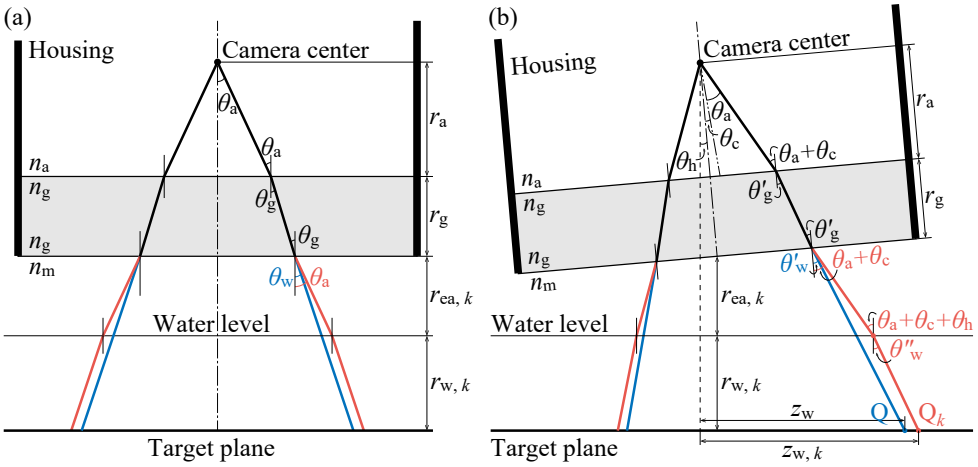

Fig. 3. Effects of the camera tilt angle and the housing tilt angle on the field of view of the UHI instrument due to assembly error. (a) Light paths of a certain pixel without assembly error, and (b) with assembly error. The angles θ_a and θ_w denote the incident angle of the pixel in air and water, respectively. The angles θ'_g, θ'_w and θ''_w denote the corresponding refraction angles in the optical window and in water considering the tilt angle of camera θ_c and the tilt angle of housing θ_h, respectively. With the water depth of $r_{w,k}$ and the air layer between glass and water surface of thickness $r_{ea,k}$, the target point Q_k covered by pixel P is located $z_{wa,k}$ away from the center in the target plane. With the water depth $r_w = r_m$, the UHI instrument is submerged and the target point Q covered by pixel P is located z_w away from the center in the target plane. The scale of the housing is exaggerated compared with the external light paths, which tend to be 1~2 orders of magnitude larger than the in-housing geometry in practical deployments.

the UHI instrument are taken into account as shown in Fig. 3(b). It's worth noting that the tilt angle component along the other axis perpendicular to the slit has the same effect on all pixels and thus can be ignored in the refraction model. The target is set to be the bottom of a water tank filled with different depths of water, as described in Sec. 2.2. With the water depth of $r_{w,k}<r_m$ and the air layer between glass and water surface of thickness $r_{ea,k} = r_m - r_{w,k}$, the target point Q_k covered by pixel P is located at

$$z_{wa,k} = \frac{r_a \sin(\theta_a + \theta_c + \theta_h)}{\cos(\theta_a + \theta_c)} + \frac{r_g \sin(\theta'_g + \theta_h)}{\cos\theta'_g} + r_{ea,k}\tan(\theta_a + \theta_c + \theta_h) + r_{w,k}\tan\theta''_w, \tag{37}$$

whereas with the water depth $r_w = r_m$, the UHI instrument is submerged and the target point Q covered by pixel P is located at

$$z_w = \frac{r_a \sin(\theta_a + \theta_c + \theta_h)}{\cos(\theta_a + \theta_c)} + \frac{r_g \sin(\theta'_g + \theta_h)}{\cos\theta'_g} + r_w\tan(\theta'_w + \theta_h) \tag{38}$$

with

$$\theta'_g = \arcsin\frac{n_a \sin(\theta_a + \theta_c)}{n_g} \tag{39}$$

$$\theta'_w = \arcsin\frac{n_a \sin(\theta_a + \theta_c)}{n_w} \tag{40}$$

$$\theta''_w = \arcsin\frac{n_a \sin(\theta_a + \theta_c + \theta_h)}{n_w} \tag{41}$$

Optics EXPRESS

where θ_a denotes the incident angle of the pixel in air depending on the position of the pixel on the sensor and the focal length; θ'_g, θ'_w and θ''_w denote the corresponding refraction angles in the optical window and in water considering the tilt angle of camera θ_c and the tilt angle of housing θ_h, respectively. The tilt angles are assumed to be small such that the vertical changes in the refractive interface attributed to different tilt centers are negligible, i.e., all the tilt centers lie on the symmetry axis of the UHI instrument.

The corresponding pixel P_k that receives light from target point Q at water depth $r_{wa,k}$ can then be found by linear interpolation of the pixel index based on Eq. (37) and Eq. (38).

3. Experiments and results

3.1. Radiometric flat field calibration in air

An underwater hyperspectral imager (UHI-4, SN/4-10, Ecotone, Norway) was used throughout this study as the UHI instrument to be calibrated. The UHI-4 is a push-broom hyperspectral imager which has a spatial resolution of 1936 pixels covering a full angle field of view of 70° in air (approx. 50° in water), and a spectral resolution of 832 channels in the range of 380~750 nm.

First, a radiometric flat field calibration was performed, which aims to determine the coefficient ρ in Eq. (21) for each pixel of the UHI-4 to correctly convert the raw digital values DN_a to radiance S_a. The calibration was conducted in air as shown in Fig. 4 by measuring a uniform light field with constant broadband radiance to eliminate geometric and electrical differences between pixels.

A 5.3-inch integrating sphere (819D-IS-5.3, Newport, USA) with Spectralon (Polytetrafluoroethylene or PTFE, Labsphere, USA) coating was used along with a xenon fiber light source (LQX1000, Linos, Germany) to provide the uniform light field for the calibration. There were three orthogonal ports on the top, front and side of the integrating sphere, which were used for light source input, UHI-4 measurements and reference monitoring, respectively. Light was introduced into the integrating sphere by optical fiber through a SubMiniature version A (SMA) connector fiber-optic adaptor mounted to the 1-inch port on top. The UHI-4 was firmly supported by a stand, facing the 2.5-inch port in front of the integrating sphere. A spectrometer (USB4000, Ocean Optics, USA) was connected via optical fiber to the 1-inch port on the side to monitor the radiance in the sphere during the calibration, where the spectrometer was calibrated by the RAMSES ARC-VIS spectroradiometer in advance.

The hyperspectral sensor of the UHI-4 along with an 8 mm lens (M0814-MP2, Computar, Japan) was sealed in the housing with its center located approximately 5 cm behind the 3 cm thick optical window which produces a field of view exceeding the 2.5-inch port of the integrating sphere. Instead of replacing the sphere with a larger one, a segmented approach was used where the integrating sphere was mounted on a turntable and manually rotated around the center to which the UHI-4 was fixed as shown in Fig. 4(a). The UHI-4 measured continuously while the integrating sphere stopped at ten fixed angles covering 90° with an interval of 10° to illuminate a segment of the sensor at a time as shown in Fig. 4(b). In each scanned swath, the bright segment corresponds to the captured bright strip of the integrating sphere and the illuminated area on the UHI-4 sensor as shown in Fig. 4(c). A time sequence of the scanned swaths as shown in Fig. 4(e) clearly recorded the measured light field at the ten stops of the integrating sphere. At each fixed angle, 40 scans in the middle section as marked by colored bands in Fig. 4(e) were selected and averaged to reduce random errors. Figure 5(a) shows example of typical raw readings DN_a of the UHI-4 corresponding to the segments. The overlapping segments were combined by taking the average of the maximum 2% (threshold determined via experiments) values as a single value at every specific wavelength and spatial pixel. The combined results are shown in Fig. 5(a) and (b) as thin black curves, and were used as equivalents of the response of the entire sensor. The raw data DN_a was also processed by the default factory calibration coefficient to obtain S_a as shown in Fig. 5(b) for comparison. It can be seen from Fig. 5 that the integrating sphere produced

Optics EXPRESS

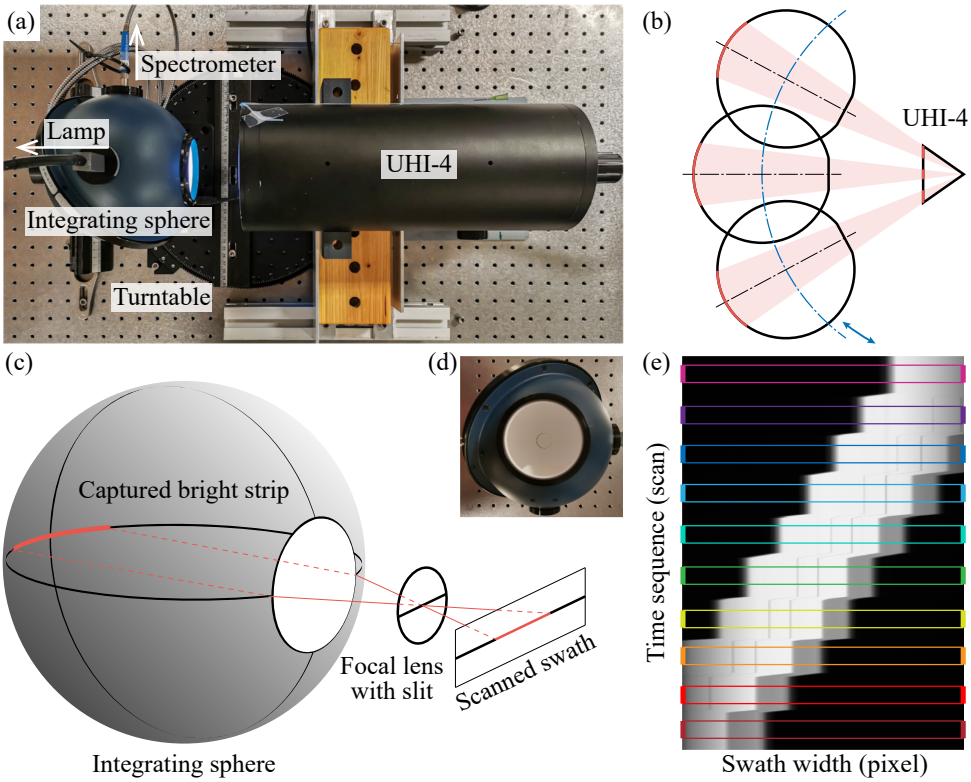

Fig. 4. Experiments of the radiometric flat field calibration in air. (a) Platform of the experiments. (b) Simplified schematic of the segmented calibration method where the integrating sphere rotates on the turntable to fulfill the field of view of the UHI-4 fixed at the rotation center. (c) A segment of the scanned swath was illuminated at a time. (d) The reflective-coated plug blocking the opposite port created a dark seam around the edge shown as two dark stripes in the scanned swath. (e) Time sequence of the scanned swaths. The illustrated intensities were summed across all wavelengths. The colored bands mark the scans with the integrating sphere at the fixed angles to be averaged for the segments and plotted in Fig. 5 with curves of the same colors. The data scanned during transition of the integrating sphere between angles was discarded.

Optics EXPRESS

a uniform light distribution such that the segments were continuous and consistent with each other. The segments were then spliced in spatial and spectral dimension to represent the response of the entire UHI-4 sensor. By definition of the radiometric flat field calibration, the spliced response of each spatial pixel at a certain wavelength DN_a was converted to the same radiance L_a of the light source, e.g., the spliced curve in Fig. 5(a) was calibrated to a flat line. In contrast, as can be seen from Fig. 5(b), the default calibration does not produce a flat response. Effects of an inhomogeneous light source and misaligned integrating sphere track in relation to different UHI-4 postures on the consistency of the flat field calibration are discussed in Sec. 5.1.

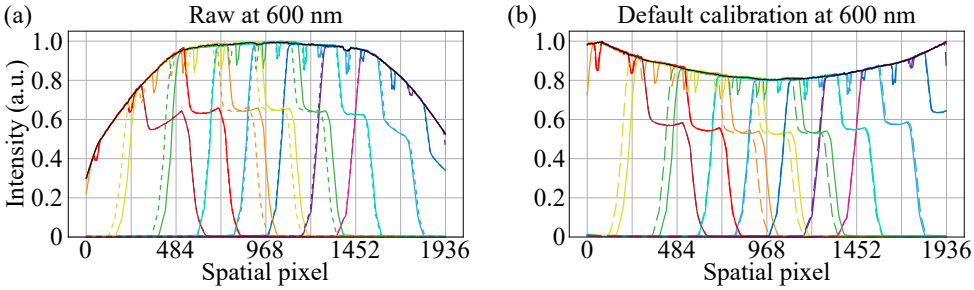

Fig. 5. Segments measured during the radiometric flat field calibration. The segments were presented in the form of (a) raw data DN_a and (b) processed data S_a by the default calibration at the wavelength of 600 nm for example. The rotational experiment was conducted in both clockwise (solid lines) and counterclockwise (dash lines) to reduce operating errors, and the color of the curves correspond to the colored bands in Fig. 4(e). The overlapping segments were combined as equivalents of the response of the entire sensor shown in thin black curves.

3.2. *Refraction model considering tilt angle caused by assembly error*

As a prerequisite for the pixelwise immersion factor calibration of the UHI-4, experiments were conducted to build the refraction model according to Eq. (37) and Eq. (38). The first step was to find out the actual position of the center of the UHI-4 sensor in the housing as shown in Fig. 6(a). A printed strip pattern with 1 mm thick strips and 1 cm interval between strips on a paper screen was used as the target. The target was mounted on a carrier which moved along a track parallel to the UHI-4. The target was imaged by the UHI-4 at 12 distances to capture even numbers (between 12 and 34) of strips in a series of images, such that the swath width $w = 11, 13, \ldots, 33$ cm. The corresponding distance r_m between UHI-4's front window and the target along the track was measured with a caliper (with accuracy of 0.05 mm). The thickness of the optical window r_g given in the specification was 3 cm. According to the invariance of viewing angle and similar triangles, the distance r'_a between the equivalent camera center C′ and the optical window was determined by linear regression of the strip-distance pairs to be 1.29 cm as shown in Fig. 6(b). The second step was to determine the tilt angle of the camera θ_c and the tilt angle of the housing θ_h relative to the actual assembly. The experimental schematic is shown in Fig. 7(a), and the platform is shown in Fig. 7(b). The nominal viewing angle of each pixel θ_a of the UHI-4 in air was calculated based on the physical size of the sensor (11.314 mm) and the focal length (8 mm) of the lens according to specifications of the instrument. Distortion of the lens system is beyond the scope of this study, and was assumed to be negligible.

The refraction model was built for pure water and for seawater with 35 psu salinity separately. The pure water used in the experiment was produced by an ultrapure lab water purification system (Milli-Q, Merck, Germany) generating 0.2 μm filtered and deionized water. The 35 psu seawater was prepared by dissolving 350 g sodium chloride in 10 liters of deionized water. The refraction models also involved the refractive indices of pure water and the 35 psu seawater [32], and the

Optics EXPRESS

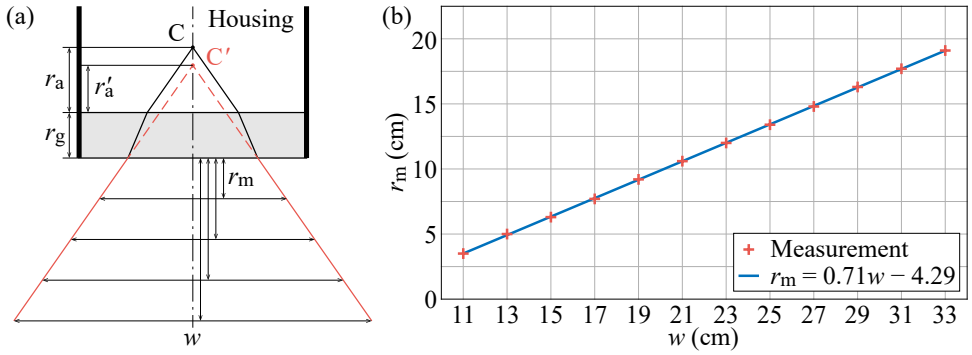

Fig. 6. The actual camera center C was determined through experiments. (a) Images of a printed strip pattern were taken at different distances r_m to cover different swath widths w. Point C′ denotes the equivalent camera center due to refraction through the optical window of thickness r_g. The distances from C and C′ to the optical window are represented by r_a and r'_a, respectively. (b) The distance r'_a was estimated by linear regression of r_m and w according to the invariance of viewing angle and similar triangles.

refractive index of the optical window made of fused silica [33]. Four repeated experiments were conducted using pure water, and four repeated experiments were conducted using the 35 psu seawater. The procedures and results of the experiments in pure water are explained in detail below.

A halogen lamp (HLX 64657, Osram, Germany) driven by a DC power supply (ES300, Delta Elektronika, Netherlands) at constant 21 V and 10 A was used as the light source. A custom water tank was placed on a frame above the halogen lamp. A 200×200×1.25 mm white diffusing glass (#34-481, Edmund Optics, USA) was fixed under the water tank to evenly distribute light at the bottom. A translucent plastic sheet carved with an array of 1×1 cm lattices was used as a mask to create a spatial pattern at the water tank bottom for the refraction experiment. The hyperspectral image of the mask taken by the UHI-4 was summed over the wavelength range to provide a spatial distribution of alternating light and dark stripes pattern indexed by the pixel numbers. The imaged stripes pattern expands as shown in Fig. 7(c) with the water depth increased from 1 cm to 7 cm since the field of view of the UHI-4 decreases as the water depth increases due to refraction. When the water depth gradually increased to submerge the UHI-4 during the experiment, air bubbles were trapped in front of the optical window due to the flange design of the housing. The trapped air bubbles were thoroughly extracted through a PTFE tubing fixed to the side of the UHI-4 with a syringe. However, this is only a problem at shallow depths, as pressure squeezes the air bubbles in deep water deployments.

As the mask was placed at a fixed position, a coordinate system was established, and each pixel on the UHI sensor was associated with a target point on the bottom of the water tank through the refraction model presented in Sec. 2.3. For quantitative comparison, the imaged stripe patterns were normalized by dividing the sum of the corresponding hyperspectral images without mask to mitigate the difference in brightness, followed by subtraction of the mean and division by the standard deviation. The original stripe patterns imaged at different water depths are shown in the upper part of Fig. 7(d), and were transformed using the refraction model based on Eq. (37) and Eq. (38) as a function of θ_c and θ_h to predict the stripes pattern at the (submerging) water depth of 7 cm. The predicted and measured stripe patterns at 7 cm water depth were compared using the Pearson correlation coefficient (PCC) as a metric. A grid search was performed to find out the combination of θ_c and θ_h that maximizes the mean PCC over the predictions of the submerging stripes pattern from 1∼6 cm water depths and the four repeated experiments.

Optics EXPRESS

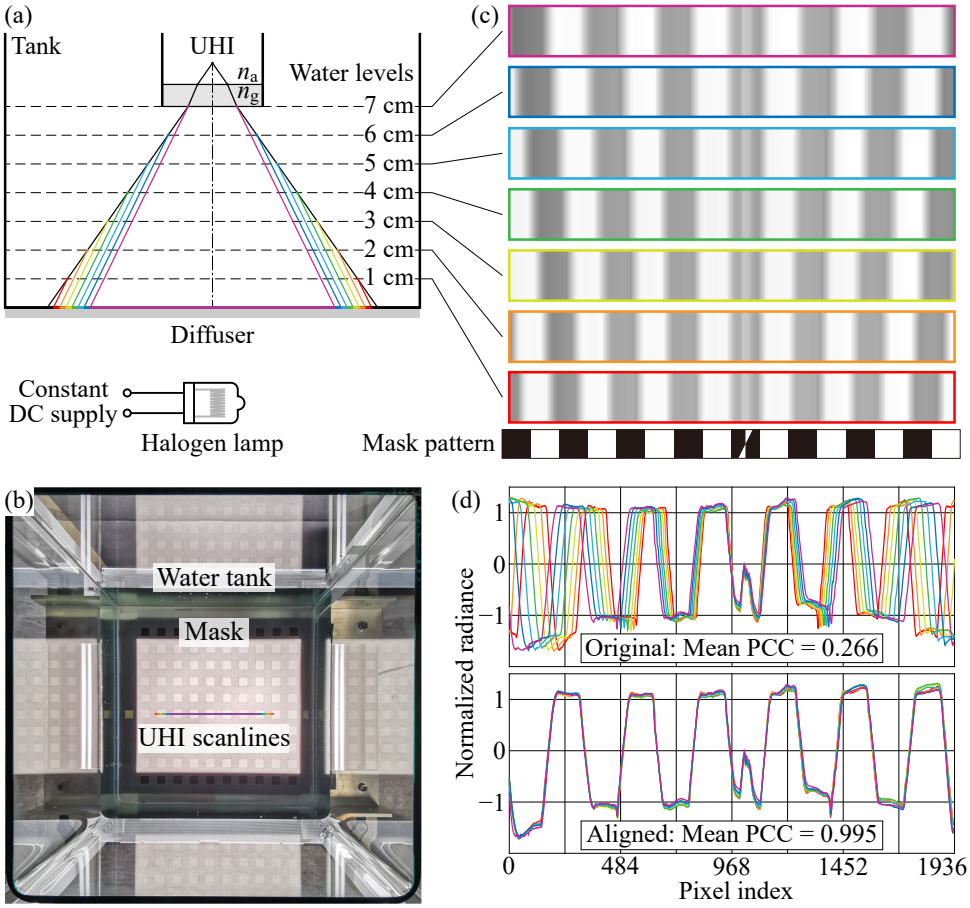

Fig. 7. Experiments for building the refraction model. (a) Schematic of the refraction and experiments. Light paths with refraction at different water depths are in different colors. (b) Top view of the experimental setup. (c) Spectral sum of the UHI-4 images of the mask pattern as alternating light and dark stripes. (d) The original stripe patterns measured at 1~6 cm water depths in the upper part were transformed using the refraction model with the optimized θ_c and θ_h for predictions to match with the measured patterns at 7 cm water depth as shown in the lower part. The UHI-4 swaths in (b), the stripe patterns in (c) and the curves in (d) are all in the corresponding colors as in (a) for different water depths.

Optics EXPRESS

Results of the grid search for pure water are shown in Fig. 8(a) where the optimized combination is θ_c = -2.0° and θ_h = 0°. Figure 8(b) shows the effect of θ_c on the mean PCC over the predictions of the submerging stripes pattern from 1~6 cm water depths at a fixed θ_h = 0° in one of the four repeated experiments. By substituting the optimized combination of θ_c and θ_h into Eq. (37) and Eq. (38), the predicted submerging stripe patterns were aligned as shown in the lower part of Fig. 7(d) with the mean PCC of 0.995. The same procedures were also performed for the 35 psu seawater, and the grid search also yielded the optimized combination of θ_c = -2.0° and θ_h = 0°.

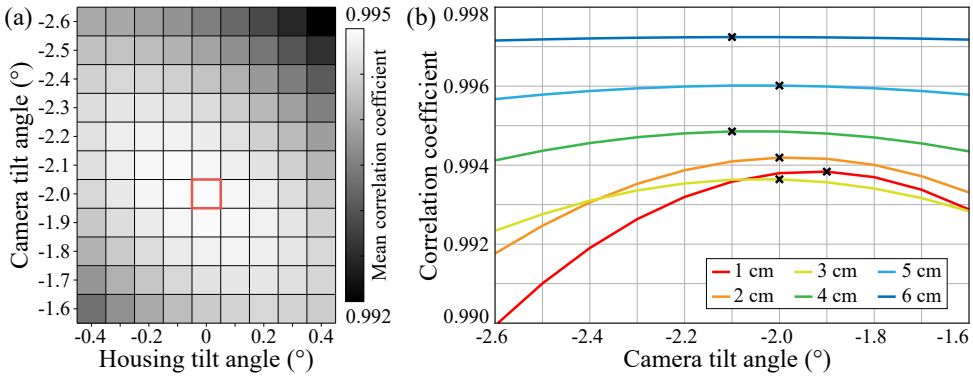

Fig. 8. Results of the grid search to optimize the camera tilt angle θ_c and housing tilt angle θ_h of the UHI-4 in pure water. (a) The combination of θ_c and θ_h that maximizes the mean PCC over the predictions of the submerging stripes pattern from 1~6 cm water depths and the four repeated experiments is marked by the red box. (b) PCCs at different θ_c and a fixed θ_h = 0° in one of the four repeated experiments.

3.3. *Immersion factor of the point-sampling spectroradiometer*

Immersion factor of the RAMSES ARC-VIS spectroradiometer was experimentally determined by repeating Zibordi's method [27,28] to verify the reliability of the platform. The experiment was repeated four times in pure water and four times in 35 psu seawater both at 26°C, and the water was completely replaced each time to avoid airborne particles and light bulb heating. The immersion factor determined using the experimental platform was compared with Zibordi's results [28] in pure water and 35 psu seawater at 20°C as shown in Fig. 9. As a reference, Austin's theoretic immersion factor was calculated by Eq. (14) with the refractive index of pure water [32] and the refractive index of the optical window made of fused silica [33]. The immersion factor provided by the manufacturer was also added for comparison.

In pure water, the measured immersion factor was consistent with Zibordi's results and that provided by the manufacturer. In the 35 psu seawater, the measured immersion factor was 0.5% higher than Zibordi's results at 400 nm, and they gradually converge at longer wavelengths. The divergence could be explained by the difference in temperature and difference between instruments, since the two curves of the immersion factor measured in pure water and seawater were consistent in trend and approximately parallel. The same pattern was also found in Zibordi's results between the two curves in pure water and the 35 psu seawater. At this point, the experimental platform was verified to be reliable for immersion factor calibration.

3.4. *Immersion factor of the push-broom hyperspectral imager*

The immersion factors of the UHI-4 for pure water and 35 psu seawater were determined experimentally using the same platform described in Sec. 3.2 without the carved mask. The refraction model determined in Sec. 3.2 was used to align the measured radiance at different

Optics EXPRESS

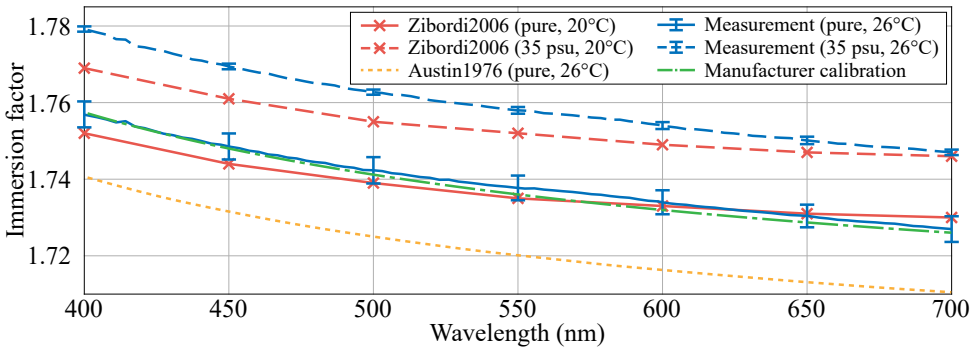

Fig. 9. Immersion factor of the RAMSES ARC-VIS spectroradiometer was determined experimentally to verify the reliability of the platform.

water depths in the immersion factor calibration. According to Zibordi [27] and Eq. (36), the pixelwise immersion factor of the UHI-4 was calculated and is shown in Fig. 10. Eight repeated experiments were conducted using pure water, and seven repeated experiments were conducted using the 35 psu seawater.

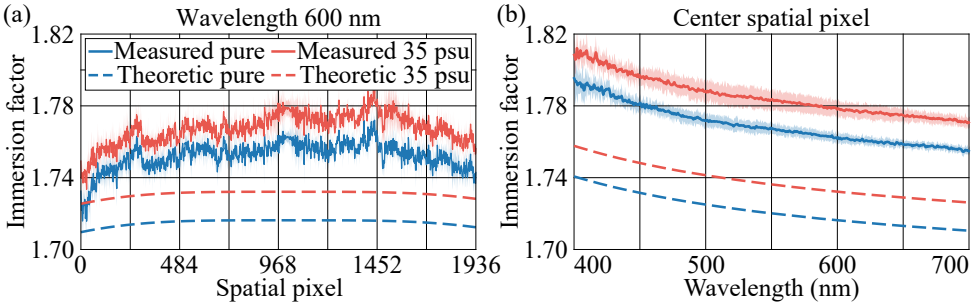

Fig. 10. Theoretically and experimentally determined immersion factor of the UHI-4 in pure water and the 35 psu seawater. Spatial properties of the immersion factor at 600 nm are shown in (a) while spectral properties of the immersion factor at the center pixel are shown in (b). The solid curves show the average immersion factor of 8 pure water or 7 seawater experiments, as indicated in legend, with the standard deviation shown with shading.

The theoretically determined immersion factors according to Eq. (26) in the two water types are also presented in Fig. 10. The pixelwise immersion factor in the spatial dimension is presented in Fig. 10(a) at 600 nm for example, and the immersion factor for the center pixel across the wavelength between 400-700 nm is presented in Fig. 10(b). The immersion factor of the center pixel of the UHI instrument was measured to be 1.763 at 600 nm in pure water, and the averaged difference in immersion factor between the center and edge pixel of the UHI instrument in the visible light band was estimated to be 1~3% across a half angle field of view of 35° in air. The measured f_{im} was notably larger than the theoretical f_{im}, which is discussed in detail in Sec. 5.2.

The above determined immersion factor of the UHI-4 in pure water was verified in two steps by measuring the water tank bottom, whose ground-truth radiance was measured by the calibrated RAMSES ARC-VIS spectroradiometer and the USB4000 spectrometer. The immersion factor of the UHI-4's center pixel was verified by comparing the f_{im}-corrected center pixel radiance with the radiance of the corresponding central area of the water tank bottom measured by the RAMSES ARC-VIS spectroradiometer. The variation pattern of the immersion factor in the spatial dimension was verified by comparing the f_{im}-corrected slit image with the radiance

Optics EXPRESS

measured by the USB4000 spectrometer along the UHI-4's swath at the bottom of the water tank as shown in Fig. 11(a).

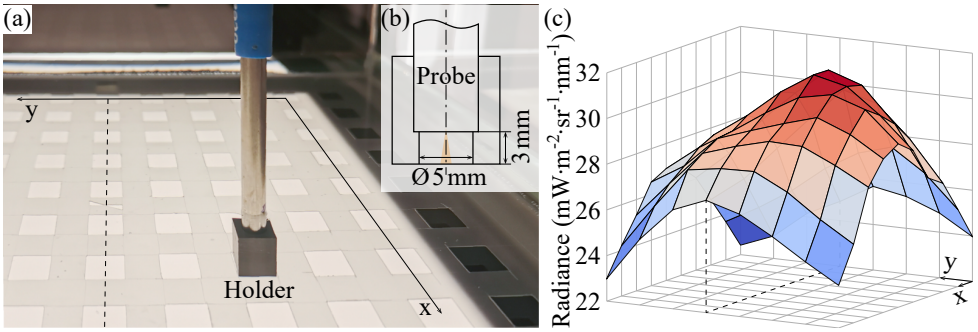

Fig. 11. The USB4000 spectrometer was used to measure the light distribution of the bottom of the water tank as the ground truth to verify the immersion factor of the UHI-4. (a) The probe of the USB4000 spectrometer was mounted on a custom holder to measure at an array of sampling points constrained by the carved mask while keeping the measuring distance. (b) Section drawing of the custom holder. (c) The light distribution of the bottom of the water tank was measured on an 8×10 array of holes. The dotted line in both (a) and (c) marks the position of the UHI-4 swath at the water tank bottom.

A custom holder was made to hold the probe of the USB4000 spectrometer at a constant height and to block lateral stray light as shown in Fig. 11(b). The square outer bottom of the probe holder matched the carved lattice of the mask so that the light distribution at the bottom of the water tank was measured on an 8×10 array as shown in Fig. 11(c). A coordinate system was established based on the mask, and the UHI-4's field of view was mapped onto it. The radiance along the UHI-4's swath was then interpolated using cubic splines based on the 8×10 sampled radiance array as the ground truth.

The radiance measured by the USB4000 spectrometer as shown in Fig. 11(c) is not directly comparable with the radiance measured by the UHI-4. Since the USB4000 spectrometer was calibrated in air and used in water in this experiment, Austin's theoretic immersion factor calculated by Eq. (14) was used to correct the radiance measured by the USB4000 spectrometer. The radiance along the UHI-4's swath was also compensated for pure water attenuation due to different path of light detected by different pixels of the UHI-4. Due to the use of a diffuser, each point on the water tank bottom is assumed to emit light evenly in all directions. Consequently, they both measured the same radiance although the probe of the USB4000 spectrometer was perpendicular to the measured surface while the UHI-4 received light from different angles.

The results of the two-step verification were presented in Fig. 12. The RAMSES ARC-VIS was fixed at the same height (approx. 7 cm) as the UHI-4 and submerged in pure water to measure the radiance of the center area of the water tank bottom, and the manufacturer provided immersion factor was used to correct the result. The radiance of the center area was also measured by the USB4000 spectrometer and corrected as explained above as a reference. As to the radiance measured by the UHI-4, the raw data DN_w along the swath was processed by four different calibration coefficients to test the effects of them compared to the reference spectrum measured by the RAMSES ARC-VIS spectroradiometer and the USB4000 spectrometer. The first was the default calibration coefficient provided by the manufacturer. The second was the coefficient of the flat field radiometric calibration. The third was the combination of the flat field calibration and the theoretic immersion factor calibration according to Eq. (26). The last was the combination of the flat field calibration and the immersion factor calibration based on measured interface reflectance and according to Eq. (36).

Optics EXPRESS

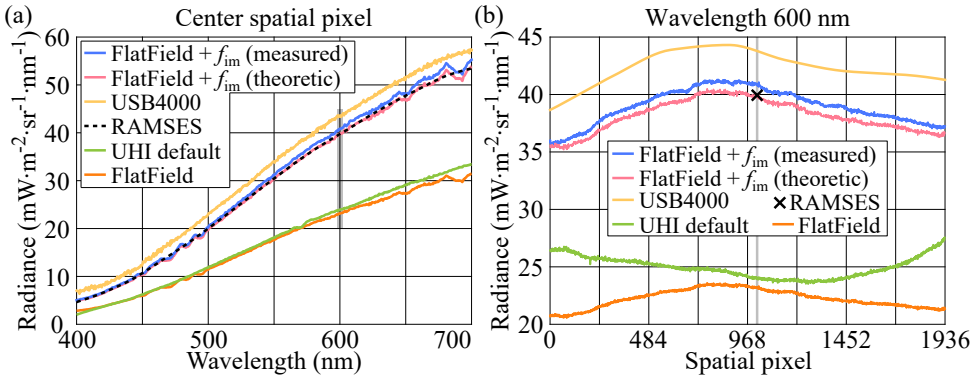

Fig. 12. Results of the two-step verification of the determined immersion factor f_{im} of the UHI-4. (a) The f_{im}-corrected center pixel radiance matched the radiance of the corresponding central area of the water tank bottom measured by the RAMSES ARC-VIS spectroradiometer. The gray line marks the section expanded spatially at 600 nm in (b). (b) The UHI-4's raw data DN_w along the swath were processed through four different calibration coefficients and compared with the ground truth measured by the USB4000 spectrometer. The RAMSES ARC-VIS spectroradiometer and the 1015th pixel of the UHI-4 measured the same target point perpendicularly, and the gray line marks the section of the 1015th pixel expanded by wavelength in (a).

As shown in Fig. 12(a), the UHI-4 measured radiance S_w processed by the default calibration coefficient (UHI-4 default) and the flat field calibration coefficient (in orange) were similar to each other and lower than the RAMSES ARC-VIS measured radiance. The UHI-4 measured radiance processed by the two f_{im}-corrected calibration coefficients (in pink and blue, respectively) were similar and matched well with the RAMSES ARC-VIS measured radiance, which verified the theoretically and experimentally determined immersion factor of the UHI-4's center pixel. Note that there is a gap between the USB4000 spectrometer measured radiance and the RAMSES ARC-VIS measured radiance possibly due to the overestimated immersion factor of the USB4000 spectrometer.

As to the variation pattern of the immersion factor in the spatial dimension, the radiance along the swath measured by the UHI-4 and processed by the four calibration coefficients were compared with the ground truth measured by the USB4000 spectrometer as shown in Fig. 12(b). All curves have similar shape except the UHI-4 default result (in green), showing the flat field radiometric calibration contributed significantly to the accuracy. To quantitatively evaluate the measured f_{im} in the spatial dimension, the f_{im} (measured) corrected UHI-4 radiance and the ground-truth radiance measured by the USB4000 spectrometer were first normalized by subtraction of the mean and division by the standard deviation. The root mean square error between them was then calculated as shown in Fig. 13 at typical wavelengths between 450-700 nm for instance. Results show that the normalized f_{im} (measured) corrected UHI-4 radiance matches the normalized USB4000 radiance with the root mean square errors less than 0.25.

Optics EXPRESS

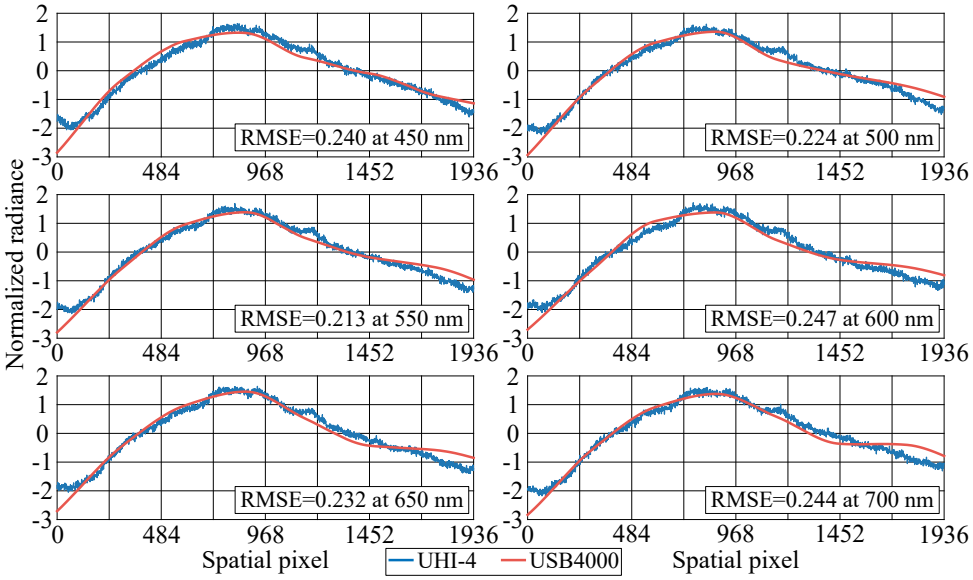

Fig. 13. Comparison between the immersion factor f_{im} (measured) corrected UHI-4 measured radiance along the swath at the bottom of the water tank and its ground-truth radiance measured by the USB4000 spectrometer at typical wavelengths between 450-700 nm. The f_{im} (measured) corrected UHI-4 radiance and the USB4000 radiance were first normalized by subtraction of the mean and division by the standard deviation, and the root mean square error (RMSE) between the normalized UHI-4 and USB4000 radiance was then calculated to prove that the variation pattern of the determined immersion factor f_{im} (measured) in the spatial dimension was correct.

4. Application to field data from an Arctic ice algae survey

The experimentally determined immersion factor of the UHI-4 was applied to a dataset of a UHI survey of ice algae under Arctic sea ice as a case study. The dataset was collected by the UHI-4 equipped on a double Blueye remotely operated vehicle (ROV) system [34] during a seasonal investigation of the northern Barents Sea and adjacent Arctic Basin in May 2021 (Nansen Legacy cruise Q2). The survey area is shown in Fig. 14(a), and the deployment of the ROV system in Fig. 14(b). Two synchronized RAMSES ACC-VIS irradiance sensors were used to measure the downwelling irradiance above sea ice (air measurements from a tripod) and under sea ice in water (mounted on top of the ROV besides the UHI-4), respectively.

Apart from the hyperspectral imager, the UHI-4 has an RGB camera mounted next to it to record RGB images whose field of view overlaps the hyperspectral slit footage. A photogrammetry model was built upon the RGB images using structure from motion (SfM) method to provide simultaneously estimated UHI-4 pose and the 3-D model of the scene as shown in Fig. 15(a). The photogrammetry model was then used to yield a 3-D georegistration for each spectral measurement of the UHI-4 by ray casting [35].

A frame of the UHI-4's footage with a clear boundary of ice algae and sea ice in the scene was selected from the transect for further analysis. The selected slit image was divided into two areas as shown in Fig. 15(b), where the algae area has clusters of ice algae and the reference area has very low algal biomass. The UHI-4 measurement at each pixel along the slit was processed with the calibration coefficients with and without immersion factor correction for comparison. The light attenuation through Arctic water was compensated using the absorption coefficient of pure water [36] and the distance between the UHI-4 and sea ice (typically 0.8~1.0 meter) for

Optics EXPRESS

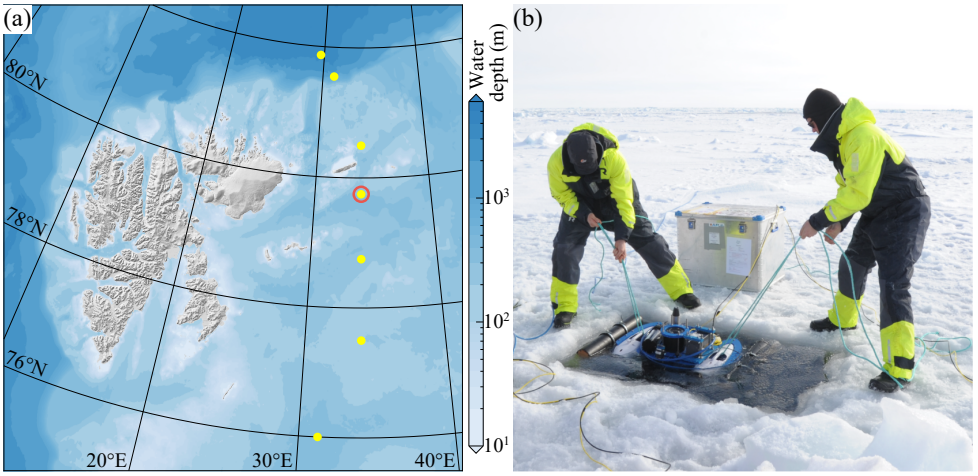

Fig. 14. Field deployment of the UHI-4 carried by a double Blueye ROV system during a seasonal investigation (Nansen Legacy cruise Q2) of the northern Barents Sea and adjacent Arctic Basin in May 2021. (a) The analyzed transect data was collected at the ice station P4 marked by red circle among the process stations marked by yellow points. (b) The transmitted spectral radiance under sea ice was measured by the UHI-4 mounted on top of the ROV, along with the downwelling irradiance above (in air) and under sea ice measured by two synchronized RAMSES ACC-VIS instruments.

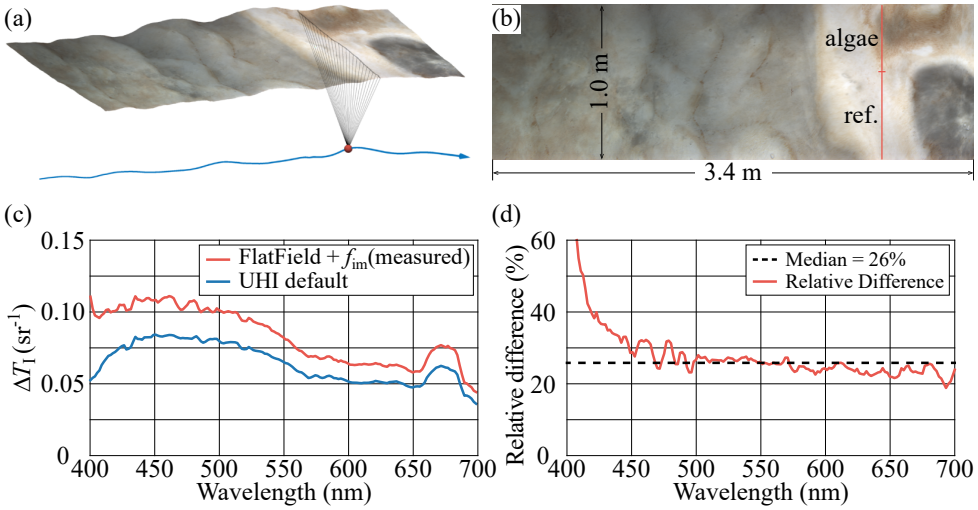

Fig. 15. Application of the calibrated immersion factor to the transect data measured by the UHI-4 during the Arctic ice algae survey. (a) Georeferenced transect of the UHI survey where the UHI-4's pose and the 3-D model of the scene was estimated using a photogrammetry model based on RGB images. (b) The selected frame of the UHI-4's footage was divided into ice algal area and reference area indicating sea ice with low concentration of ice algae. (c) Difference spectra ΔT_I based on transflectance spectra $T_{I,\,ref} - T_{I,\,algae}$, indicating *in vivo* light absorption by ice algal pigments (dominated by chlorophyll *a* and fucoxanthin). $T_{I,\,ref}$ and $T_{I,\,algae}$ represent the spectral transflectance averaged over the pixels of the sea ice and ice algae area in the slice marked in red in (b), respectively. (d) Relative difference between the ΔT_I calculated with the proposed radiometric and immersion factor calibration coefficients and the default calibration coefficients.

Optics EXPRESS

each pixel. Spectral transflectance T_I (in sr^{-1}) [37] was calculated as the ratio of the transmitted radiance L_T (in $mW{\cdot}m^{-2}{\cdot}sr^{-1}{\cdot}nm^{-1}$) measured by the UHI-4 under ice and the downwelling surface irradiance E_d (in $mW{\cdot}m^{-2}{\cdot}nm^{-1}$) measured by the RAMSES ACC-VIS irradiance sensor above ice:

$$T_I(\lambda) = \frac{L_T(\lambda)}{E_d(\lambda)}. \tag{42}$$

The RAMSES ACC-VIS has 112 spectral channels while the UHI-4 has an inherent 832 channels in the spectral range 380-750 nm. Considering optical efficiency, the UHI-4 was set up to use 208 channels (via spectral binning) for field data acquisition. The irradiance E_d was linearly interpolated in spectral dimension to align with the radiance L_T for transflectance calculation.

The difference spectrum ΔT_I was then calculated by subtracting the average spectral transflectance of the pixels in the algae area $T_{I,\,algae}$ from the average spectral transflectance of the pixels in the reference (ice) area $T_{I,\,ref}$, indicating light absorption by pigments, dominated by chlorophyll *a* (maximum absorption at 440 nm and 673 nm) and fucoxanthin providing an absorption shoulder from 440~535 nm [2]. As shown in Fig. 15(c) and (d), the difference spectrum $\Delta T_I = T_{I,\,ref} - T_{I,\,algae}$ increased by a median of 26% after the proposed radiometric and immersion factor calibration compared to the results with default calibration.

It's also worth noting that the *in vivo* absorption peak of chlorophyll *a* is prominent near 673 nm in the difference spectra ΔT_I in Fig. 15(c) which is due to the presence of ice algae clusters (high biomass indicted by chlorophyll *a*). Diatoms typically have a red chlorophyll *a in vivo* absorption peak of 673~675 nm [2]. It is also typical for brown macroalgae to have high absorption at around 674 nm as measured with the UHI-4 and a spectrophotometer [5].

5. Discussion

5.1. Consistency of the segmented flat field calibration

The flat field calibration presented in Sec. 2.2 was conducted with the integrating sphere rotated to build the segments as shown in Fig. 16(a). It was assumed that the same area in the integrating sphere was imaged at different angles to fulfill the entire field of view of the UHI-4. However, the rotation center of the integrating sphere cannot be guaranteed to ideally coincide with the camera center, and the homogeneity of the light coming out of the integrating sphere could be affected by subtle differences in the reflective surface and the 2.5-inch wide open port.

Therefore, different segment building approaches were tested to evaluate the consistency of the segmented flat field calibration. Other than the rotational movement, the integrating sphere was moved along a straight track. The translational movement of the integrating sphere ensured each UHI-4 segment to image a different area of the reflective surface as shown in Fig. 16(b)-(d). The straight track was fixed at the same distance (5 cm) to the UHI-4 as in the rotational experiment. Besides, the UHI-4 was placed in different postures (i.e., yaw 10° counterclockwise, pitch 2.5° clockwise, and roll 10° counterclockwise) to test their effects on the captured segments. A closer distance (4 cm) and a tilted track were also tested.

Segments for each test were spliced across the entire spatial dimension and plotted at typical wavelengths between 400-700 nm in Fig. 16(e). Results of the rotational experiment were also plotted for comparison. The spliced segments captured by different integrating sphere movements and UHI-4 postures were continuous and consistent with each other. It proved that the light coming out of the integrating sphere was uniform and stable, and the segmented flat field calibration was reliable.

As an opposite example, an inhomogeneous light distribution was created by bypassing baffles in the integrating sphere. The segments imaged by the UHI-4 are shown in Fig. 17, where the curves for different segments are not consistent with each other in the overlapping regions.

Optics EXPRESS

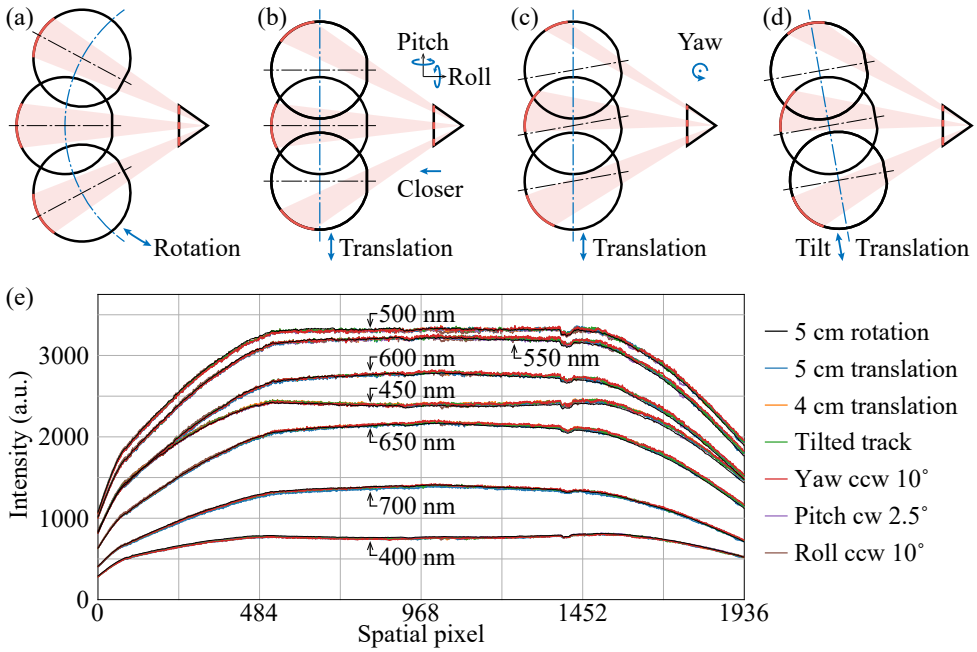

Fig. 16. Flat field calibration by different segment building approaches. Segments were captured with different integrating sphere tracks and UHI-4 postures illustrated in (a)-(d) where different regions of the imaged reflective surface were marked with red shading. (e) The spliced segments from different cases were continuous and consistent in the entire spatial and spectral dimensions.

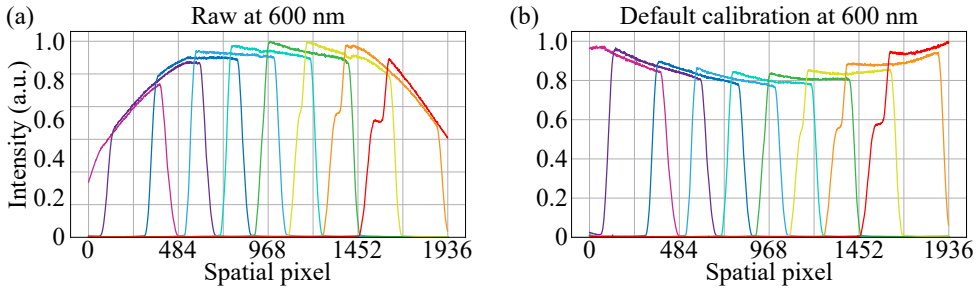

Fig. 17. Segments measured with the light not evenly distributed in the integrating sphere. The different segments are not continuous in either (a) the raw data DN_a or (b) processed data S_a by the default calibration coefficients, e.g., at the wavelength of 600 nm.

Optics EXPRESS

5.2. Difference between the theoretic and experimental immersion factors

In the results of the immersion factor f_{im} calibration of the RAMSES ARC-VIS spectroradiometer as shown in Fig. 9, there is an underestimate of 1.07% of the spectral average theoretic f_{im} compared to that of the measured f_{im}. As well explained in literatures [27,28], the bias was attributed primarily to the reflection of the sensor and secondarily to the approximation of the finite solid angles.

There is also a difference between the theoretic and measured f_{im} for the UHI-4 as shown in Fig. 10. The averaged absolute relative difference between the theoretic and measured f_{im} of the UHI-4 over all spectral and spatial pixels was 2.08% for pure water. However, this underestimation can not be explained by the multiple reflection in the optical window or the reflection of the UHI-4 sensor, since the reflected light will no longer reach the pixel at the same angle. So the bias is mainly attributed to the underestimated transmittance at the external interface of the optical window due to the approximation of the refractive index.

Another possible way to explain the difference between the measured and theoretic f_{im} for the UHI-4 was discovered through comparing Eq. (26) and Eq. (36). When the theoretic f_{im} is modified by dividing the transmittance at the water-air interface $T_{wa}(\theta_w)$, as shown in Fig. 18, the modified theoretic f_{im} matches the measured f_{im} better for both pure water and the 35 psu seawater. After modification, the averaged absolute relative difference between the measured and theoretic f_{im} decreased to 0.06%. For the 35 psu seawater, the averaged absolute relative difference decreased from 2.03% to 0.12%. It might be because even though the UHI-4 is submerged in water with no visible air bubble in front of the optical window, there still exists a thin layer of air (at molecular scale) between the optical window and the water due to possible hydrophobicity, where the transmittance at the water-air micro interface also takes effect in Eq. (24) and Eq. (26).

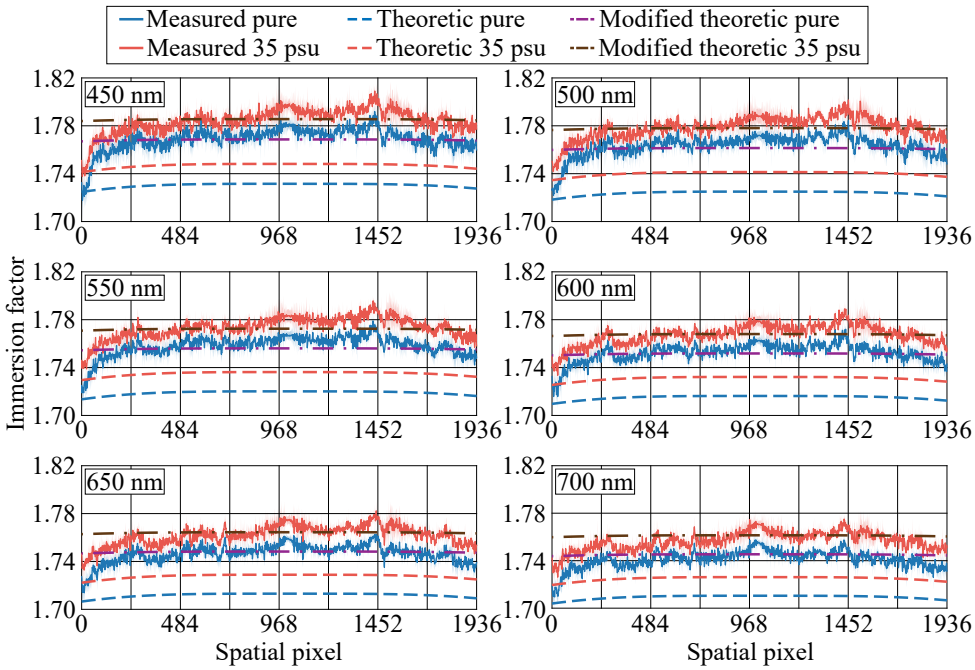

Fig. 18. The modified theoretic immersion factor of the UHI-4 is more consistent with the experimental results in terms of magnitude at typical wavelengths in both pure water and 35 psu seawater.

Optics EXPRESS

5.3. Effects of keystone and smile distortions

Spatial and spectral distortions of the UHI-4 impact on the accuracy of UHI measurements. Typical distortions are keystone and smile effects, where keystone effect is the spatial distortion as a function of wavelength which results in skewed spatial features, and smile effect is the spectral distortion as a function of slit height (spatial axis) which leads to curved spectral lines [38]. The keystone and smile distortions of the UHI-4 were quantified by using the geometric control point (GCP) method [23,39].

A series of fixed spatial and spectral features in the scene were imaged by the UHI-4 as control points with known geometric positions in the image. For instance, the printed target with the pattern of 1 mm thick strips and 1 cm intervals was used to provide spatial troughs in the image. A mercury vapor fluorescent lamp (DULUX S 11W/41-827, Osram, Germany) was used to illuminate the target to provide spectral peaks. The captured hyperspectral image is shown in Fig. 19 with the spectrum of the lamp to the right. The selected spectral peaks are annotated in the figure with their corresponding wavelengths measured by the USB4000 spectrometer as ground truth. By visual inspection, no significant keystone or smile distortion was observed from the image captured by the UHI-4.

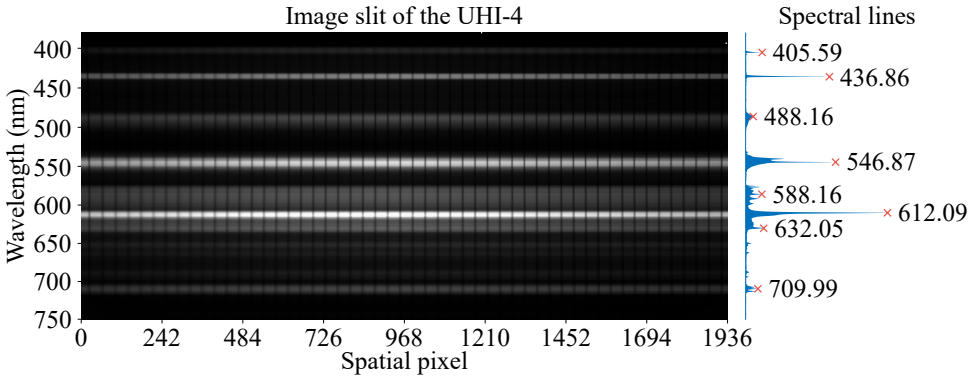

Fig. 19. Hyperspectral image of the stripe patterns illuminated by the fluorescent lamp for the geometric control point (GCP) distortion correction. The spectrum of the lamp is measured by a USB4000 spectrometer and plotted to the right as reference. The spectral peaks selected as GCPs are marked with red crosses and their wavelengths.

A two-dimensional quadratic polynomial distortion model was used to simultaneously characterize the keystone and smile effects as

$$\mathbf{x} = \sum_{i,j=0}^{i+j\le 2} a_{ij}\, \mathbf{x}_{\text{ref}}^{i}\, \boldsymbol{\lambda}_{\text{ref}}^{j}, \tag{43}$$

$$\boldsymbol{\lambda} = \sum_{i,j=0}^{i+j\le 2} b_{ij}\, \mathbf{x}_{\text{ref}}^{i}\, \boldsymbol{\lambda}_{\text{ref}}^{j}, \tag{44}$$

where $\mathbf{x}_{\text{ref}}$ and $\boldsymbol{\lambda}_{\text{ref}}$ denote vectors of the reference coordinates in spatial and spectral dimensions, respectively, of the selected GCPs; the corresponding measured coordinates of the GCPs according to Fig. 19 are denoted by $\mathbf{x}$ and $\boldsymbol{\lambda}$. Coefficients a_{ij} and b_{ij} carry the relationship between distorted coordinates and reference coordinates of the GCPs, and were then determined by using linear least squares fitting.

The results of the GCP detection are shown in Fig. 20. For smile effect, the averaged offset in spectral dimension is less than 0.9 nm over the entire spatial range as shown in Fig. 20(a). As to

Optics EXPRESS

keystone effect, the averaged offset in spatial dimension is less than 3.2 pixels over the 400-700 nm wavelength as shown in Fig. 20(b).

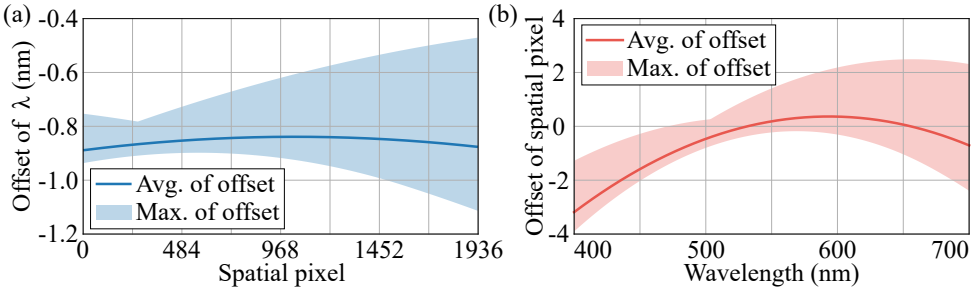

Fig. 20. Quantitative estimate of (a) the smile distortion and (b) the keystone distortion of the UHI-4 using the GCP method.

The quantitative results agreed with the visual inspection that the keystone and smile effects of the UHI-4 used in the calibration were not significant. One reason could be that the keystone and smile distortions had been calibrated by the manufacturer. Another reason could be that the target was placed close to the UHI-4 (approx. 40 cm) in the test such that the distortions were not obvious. Since the immersion factor calibration experiments were conducted at a close distance between the UHI-4 and the light source (within 30 cm), the distortions caused by keystone and smile effects were ignored in this study.

6. Conclusion

In this study, a commercial UHI instrument (UHI-4, Ecotone) was calibrated for radiometric flat field response and pixelwise immersion effect to support *in situ* measurement of absolute spectral radiance. Results showed that the proposed segmented method for radiometric flat field calibration of the UHI instrument using a small-sized integrating sphere was an inexpensive and effective alternative to the conventional method. Pixelwise immersion factor of the UHI instrument was derived theoretically and calibrated experimentally in pure water and 35 psu seawater based on the proposed refraction model which accounts for the sensor tilt due to assembly errors. The averaged absolute relative difference between the theoretic and measured immersion factor f_{im} of the UHI-4 over all spectral and spatial pixels was 2.08% for pure water and 2.03% for 35 psu seawater due to underestimated transmittance and possible hydrophobicity at the external interface. The averaged difference in immersion factor between the center and edge pixel of the UHI instrument in the visible light band was only 1~3% across its half angle field of view of 35° in air, as the angular dependence of solid angles is canceled out by the cosine effect of incident light in different media. The radiometric and immersion factor calibration of the UHI instrument was verified quantitatively through comparative experiments with the RAMSES ARC-VIS spectroradiometer (TriOS) and the USB4000 spectrometer (Ocean Optics). The calibration coefficients were used to process the spectral radiance of transmitted sunlight through ice algae clusters in sea ice measured by the UHI instrument during an Arctic under-ice bio-optical survey. After the proposed radiometric and immersion factor calibration, the difference spectra ΔT_{I} (based on transflectance spectra $T_{\mathrm{I,\ ref}} - T_{\mathrm{I,\ algae}}$) resembling *in vivo* absorption spectra of ice algae increased by a median of 26% compared to the difference spectra calculated with UHI measurements processed by the default calibration coefficients.

In future studies, the calibrated immersion factor will be used to correct hyperspectral images collected by the UHI instrument from past underwater surveys. Additionally, the calibrated UHI instrument will be deployed as an absolute spectral radiance sensor along with other radiometric instruments to facilitate accurate under-ice bio-optical mapping.

Optics EXPRESS

Funding. Universitetet i Bergen (UB100407121, UB100767101, UB100767102); Norges Forskningsråd (223254, 245923, 276730).

Acknowledgments. This work is supported by the University of Bergen through grants Annum IFT-Optikk (UB100767101), C. Saetre IFT-likestilling (UB100407121), and Annum IFT-Elektronikk og Måleteknologi (UB100767102). Geir Johnsen and Natalie Summers are funded by the Research Council of Norway (NFR) by projects the Nansen Legacy (276730), Arctic ABC Development (245923), and Centre for Autonomous Marine Operations and Systems (AMOS) (223254). The authors express their sincere gratitude to Benjamin Lange (Norwegian Geotechnical Institute) and Tristan Petit (Ifremer) for their ideas and help in the initial exploration. We would like to thank the crew of the Nansen Legacy cruise Q2 for their support in the field work. We would also like to thank Bernhard Schartmüller (UiT The Arctic University of Norway), Yifan Song (GEOMAR), and all the colleagues in the optics group at the University of Bergen, especially to Håkon Sandven, for joining discussions and providing comments. Additionally, Hongbo Liu would like to thank Yufei Jin for her encouragement and feeding. ♡

Disclosures. The authors declare no conflicts of interest.

Data Availability. Data underlying the results presented in this paper are not publicly available at this time but may be obtained from the authors upon reasonable request. The data acquisition program for the RAMSES spectroradiometers is open source, and can be found in [40].

References

1. G. Johnsen, Z. Volent, H. Dierssen, *et al.*, "Underwater hyperspectral imagery to create biogeochemical maps of seafloor properties," in *Subsea Optics and Imaging*, (Woodhead, 2013), Woodhead Publishing Series in Electronic and Optical Materials, pp. 508–535.
2. G. Johnsen and E. Sakshaug, "Biooptical characteristics of PSII and PSI in 33 species (13 pigment groups) of marine phytoplankton, and the relevance for pulse-amplitude-modulated and fast-repetition-rate fluorometry," J. Phycol. **43**(6), 1236–1251 (2007).
3. I. Dumke, S. M. Nornes, A. Purser, *et al.*, "First hyperspectral imaging survey of the deep seafloor: High-resolution mapping of manganese nodules," Remote. Sens. Environ. **209**, 19–30 (2018).
4. Ø. Sture, B. Snook, and M. Ludvigsen, "Obtaining Hyperspectral Signatures for Seafloor Massive Sulphide Exploration," Minerals **9**(11), 694 (2019).
5. N. Summers, G. Johnsen, A. Mogstad, *et al.*, "Underwater Hyperspectral Imaging of Arctic Macroalgal Habitats during the Polar Night Using a Novel Mini-ROV-UHI Portable System," Remote Sens. **14**(6), 1325 (2022).
6. A. A. Mogstad, G. Johnsen, and M. Ludvigsen, "Shallow-Water Habitat Mapping using Underwater Hyperspectral Imaging from an Unmanned Surface Vehicle: A Pilot Study," Remote Sens. **11**(6), 685 (2019).
7. F. Foglini, V. Grande, F. Marchese, *et al.*, "Application of Hyperspectral Imaging to Underwater Habitat Mapping, Southern Adriatic Sea," Sensors **19**(10), 2261 (2019).
8. I. Dumke, A. Purser, Y. Marcon, *et al.*, "Underwater hyperspectral imaging as an in situ taxonomic tool for deep-sea megafauna," Sci. Rep. **8**(1), 12860 (2018).
9. R. Pettersen, G. Johnsen, P. Bruheim, *et al.*, "Development of hyperspectral imaging as a bio-optical taxonomic tool for pigmented marine organisms," Org. Divers. Evol. **14**(2), 237–246 (2014).
10. A. A. Mogstad and G. Johnsen, "Spectral characteristics of coralline algae: A multi-instrumental approach, with emphasis on underwater hyperspectral imaging," Appl. Opt. **56**(36), 9957–9975 (2017).
11. R. Pettersen, H. Lein Braa, B. A. Gawel, *et al.*, "Detection and classification of Lepeophterius salmonis (Krøyer, 1837) using underwater hyperspectral imaging," Aquac. Eng. **87**, 102025 (2019).
12. A. Chennu, P. Färber, N. Volkenborn, *et al.*, "Hyperspectral imaging of the microscale distribution and dynamics of microphytobenthos in intertidal sediments," Limnol. Oceanogr.: Methods **11**, 511–528 (2013).
13. D. Lannuzel, L. Tedesco, M. van Leeuwe, *et al.*, "The future of Arctic sea-ice biogeochemistry and ice-associated ecosystems," Nat. Clim. Chang. **10**(11), 983–992 (2020).
14. M. A. van Leeuwe, L. Tedesco, K. R. Arrigo, *et al.*, "Microalgal community structure and primary production in Arctic and Antarctic sea ice: A synthesis," Elem. Sci. Anthropocene **6**(1), 4 (2018).
15. E. Cimoli, K. Meiners, L. Lund-Hansen, *et al.*, "Spatial variability in sea-ice algal biomass: An under-ice remote sensing perspective," Adv. Polar Sci. **28**(4), 1 (2017).
16. B. A. Lange, C. Katlein, M. Nicolaus, *et al.*, "Sea ice algae chlorophyll a concentrations derived from under-ice spectral radiation profiling platforms," J. Geophys. Res.: Oceans **121**(12), 8511–8534 (2016).
17. A. L. Forrest, L. C. Lund-Hansen, B. K. Sorrell, *et al.*, "Exploring Spatial Heterogeneity of Antarctic Sea Ice Algae Using an Autonomous Underwater Vehicle Mounted Irradiance Sensor," Front. Earth Sci. **7**, 1 (2019).
18. E. Cimoli, K. M. Meiners, A. Lucieer, *et al.*, "An Under-Ice Hyperspectral and RGB Imaging System to Capture Fine-Scale Biophysical Properties of Sea Ice," Remote Sens. **11**(23), 2860 (2019).
19. E. Cimoli, V. Lucieer, K. M. Meiners, *et al.*, "Mapping the in situ microspatial distribution of ice algal biomass through hyperspectral imaging of sea-ice cores," Sci. Rep. **10**(1), 21848 (2020).
20. G. Johnsen, A. Zolich, S. Grant, *et al.*, "All-sky camera system providing high temporal resolution annual time series of irradiance in the Arctic," Appl. Opt. **60**(22), 6456–6468 (2021).
21. S. Connan-McGinty, N. S. Banas, J. Berge, *et al.*, "Midnight Sun to Polar Night: A Model of Seasonal Light in the Barents Sea," J. Adv. Model. Earth Syst. **14**(10), e2022MS003198 (2022).

Optics EXPRESS

22. S. Grant, G. Johnsen, D. McKee, *et al.*, "Spectral and RGB analysis of the light climate and its ecological impacts using an all-sky camera system in the Arctic," Appl. Opt. **62**(19), 5139–5150 (2023).
23. M. B. Henriksen, J. L. Garrett, E. F. Prentice, *et al.*, "Real-Time Corrections for a Low-Cost Hyperspectral Instrument," in *2019 10th Workshop on Hyperspectral Imaging and Signal Processing: Evolution in Remote Sensing (WHISPERS)*, (2019), pp. 1–5.
24. C. K. Gatebe, J. J. Butler, J. W. Cooper, *et al.*, "Characterization of errors in the use of integrating-sphere systems in the calibration of scanning radiometers," Appl. Opt. **46**(31), 7640–7651 (2007).
25. A. Kokka, T. Pulli, E. Honkavaara, *et al.*, "Flat-field calibration method for hyperspectral frame cameras," Metrologia **56**(5), 055001 (2019).
26. G. McKee, S. Pal, H. Seth, *et al.*, "Design and characterization of a large area uniform radiance source for calibration of a remote sensing imaging system," in *Earth Observing Systems XII*, vol. 6677 (SPIE, 2007), pp. 62–70.
27. G. Zibordi, "Immersion Factor of In-Water Radiance Sensors: Assessment for a Class of Radiometers," Journal of Atmospheric and Oceanic Technology **23**(2), 302–313 (2006).
28. G. Zibordi and M. Darecki, "Immersion factors for the RAMSES series of hyper-spectral underwater radiometers," J. Opt. A: Pure Appl. Opt. **8**(3), 252–258 (2006).
29. A. Agrawal, S. Ramalingam, Y. Taguchi, *et al.*, "A theory of multi-layer flat refractive geometry," in *2012 IEEE Conference on Computer Vision and Pattern Recognition*, (2012), pp. 3346–3353.
30. E. Hecht, *Optics* (Pearson, 2017), pp. 123–125.
31. C. D. Mobley and R. W. Preisendorfer, *Light and Water: Radiative Transfer in Natural Waters* (Academic press, 1994), pp. 159–160.
32. R. W. Austin and G. Halikas, "The index of refraction of seawater," Technical Report SIO Reference 76-1, Scripps Institution of Oceanography, La Jolla, California (1976).
33. T. Ohde and H. Siegel, "Derivation of immersion factors for the hyperspectral TriOS radiance sensor," J. Opt. A: Pure Appl. Opt. **5**(3), L12–L14 (2003).
34. H. S. Løvås, A. J. Sørensen, and M. Ludvigsen, "Framework for Combining Multiple Lightweight Underwater Vehicles into Super Underwater Vehicle," in *2020 IEEE/OES Autonomous Underwater Vehicles Symposium (AUV)*, (2020), pp. 1–6.
35. H. S. Løvås, A. A. Mogstad, A. J. Sørensen, *et al.*, "A Methodology for Consistent Georegistration in Underwater Hyperspectral Imaging," IEEE J. Oceanic Eng. **47**(2), 331–349 (2022).
36. R. M. Pope and E. S. Fry, "Absorption spectrum (380–700 nm) of pure water II Integrating cavity measurements," Appl. Opt. **36**(33), 8710–8723 (1997).
37. M. Nicolaus and C. Katlein, "Mapping radiation transfer through sea ice using a remotely operated vehicle (ROV)," The Cryosphere **7**(3), 763–777 (2013).
38. M. B. Henriksen, E. F. Prentice, C. M. van Hazendonk, *et al.*, "Do-it-yourself VIS/NIR pushbroom hyperspectral imager with C-mount optics," Opt. Continuum **1**(2), 427–441 (2022).
39. K. C. Lawrence, B. Park, W. R. Windham, *et al.*, "Calibration of a Pushbroom Hyperspectral Imaging System for Agricultural Inspection," Trans. ASAE (2003).
40. H. Liu, "Python module to communicate with TriOS RAMSES radiometers via serial port," GitHub (2024) [accessed 9 May 2024], https://github.com/hbliu104/PyRamses.